Quaternary Science Reviews 381 (2026) 109901

Contents lists available at ScienceDirect

Quaternary Science Reviews

journal homepage: www.elsevier.com/locate/quascirev

A stormy past: long-term temperature evolution and volcanic activity as drivers of Holocene storminess in the eastern North Atlantic

J. Sjöström[a,b,c,d,*], A. Martínez Cortizas[e], A. Nylund[f], S.R. Piilo[g], L. Orme[h], R. Gyllencreutz[b,c], F. Schenk[b,c,i], R. Chiverrell[j], M. KcKeown[k,l], Claire Ansberque[b,c], M.E. Kylander[b,c]

[a] *CRETUS, EcoPast (GI-1553), Department of History, area of Archaeology, Universidade de Santiago de Compostela, 15782, Santiago de Compostela, Spain*
[b] *Department of Geological Sciences, Stockholm University, Stockholm, Sweden*
[c] *Bolin Centre for Climate Research, Stockholm University, Stockholm, Sweden*
[d] *Archaeological Research Laboratory, Stockholm University, Wallenberglaboratoriet, Stockholm, Sweden*
[e] *EcoPast (GI-1553), Faculty of Biology, Universidade de Santiago de Compostela, Santiago de Compostela, Spain*
[f] *Department of Ecology and Geoscience, Umeå University, Umeå, Sweden*
[g] *Environmental Change Research Unit (ECRU), Ecosystems and Environment Research Programme, University of Helsinki, Helsinki, Finland*
[h] *Department of Geography, Maynooth University, Maynooth, Ireland*
[i] *Department of Geosciences and Geography, University of Helsinki, Helsinki, Finland*
[j] *Department of Geography and Planning, Liverpool University, Liverpool, United Kingdom*
[k] *Department of Geography, University College Cork, Cork, Ireland*
[l] *Sustainability Institute, University College Cork, Cork, Ireland*

ARTICLE INFO

Handling Editor: Dr Mira Matthews

ABSTRACT

Understanding long-term variability in storminess is essential for constraining future climate patterns in the eastern North Atlantic, a region shaped by complex ocean–atmosphere interactions. Here, we reconstruct storm, fire, and hydroclimate variability from grain size, inorganic geochemistry, plant macrofossil and molecular organic records since mid-Holocene at Glenties Bog, a coastal blanket bog in western Ireland. Comparing our results with existing palaeostorminess records, we provide new insights into a dynamic interplay between wind strength, fire incidence, and hydrological conditions throughout the Holocene.

Long-term temperature evolution influenced the background wind and hydroclimatic state, while volcanic activity became a key forcing mechanism during parts of the late Holocene. The warm mid-Holocene coincided with lower wind strength and enhanced fire activity, while no assoication between storm periods and volcanic activity was inferred, indicating that the climate state at the time of the volcanic forcing affects the climatic response.

These results indicate that future warming may lead to profound changes in wind strength, hydroclimate, and fire regimes. Notably, climate-change-induced lowering of peatland water tables may increase the susceptibility of blanket bogs to intense and deep peatland fires.

This study provides new insight into Holocene wind and hydroclimate dynamics in the eastern North Atlantic, improving understanding of the mechanisms driving North Atlantic climate variability across contrasting climate states.

1. Introduction

Storms linked to extra-tropical cyclones can cause major societal and economic disruption, impacting infrastructure, industry and human health (e.g., Feser et al., 2015). In Europe, the weather and climate are strongly influenced by the position and intensity of the North Atlantic storm track, with storms being associated with extreme precipitation and wind events (Brayshaw et al., 2009, 2010). The storm track is in turn

---

[*] Corresponding author. CRETUS, EcoPast (GI-1553), Department of History, area of Archaeology, Universidade de Santiago de Compostela, 15782 Santiago de Compostela, Spain

E-mail address: jennykristina.sjostrom@usc.es (J. Sjöström).

https://doi.org/10.1016/j.quascirev.2026.109901
Received 12 November 2025; Received in revised form 20 February 2026; Accepted 21 February 2026

strongly linked to, and interacts with, atmospheric pressure centres, namely the tropospheric jet and the polar vortex. Storms form in regions of strong baroclinity, i.e. areas with large pressure and temperature differences, and their track is influenced by the subtropical jet and midlatitude sea surface temperature front (Brayshaw et al., 2009).

The storm intensity is strongest during winter, when the meridional temperature gradient and the jet stream reach their peak strength. The main mode of atmospheric variability in the region is the North Atlantic Oscillation (NAO), which reflects fluctuations in the pressure gradient between the Icelandic Low and the Azores High (Hurrell and Van Loon, 1997; Trigo et al., 2002) (Fig. 1). During the positive phase of the NAO (NAO+), the westerly wind pattern, including the storm track, becomes stronger and shifts northward (Pinto et al., 2009; Feser et al., 2015), bringing warm, moist air to northern Europe. In contrast, a negative phase (NAO−) weakens the westerly airflow, often leading to colder and drier winters in Europe and a southward displacement of the storm track, and wetter conditions, in the Mediterranean area (Hurrell and Van Loon, 1997; Trigo et al., 2002; Feser et al., 2015). The intensity of NAO-related pressure gradients is influenced by both the jet stream and the condition of the polar vortex (Walter et al., 2005; Kidston et al., 2015). Currently, there is low confidence in projections of how ongoing and future climate change will affect the frequency, intensity, and location of storms over Europe (IPCC, 2021), due to the complex processes controlling storm dynamics. Both storminess and the NAO are dominated by internal variability on annual to multi-decadal timescales, and their response to external forcing remains unclear. A very large multi-model ensemble shows only a weak predictive skill to external forcing on a near-decadal scale (Klavans et al., 2021). Studying storminess on longer timescales is hence crucial to infer whether external forcing has a notable impact that may help to anticipate potential future changes.

We can improve our understanding of how these complex processes affected different regions by using natural archives such as dunes, ice sheets and peatlands. By reconstructing paleostorminess and its relationship to past climate variability, we can improve our understanding of future atmospheric responses. In this study, we turn to the European west coast, and northwestern Ireland specifically, where storms make landfall at full intensity. The climate of northwestern Ireland is characterised by high annual precipitation, cool temperatures, low seasonal temperature variability, and high frequency of Atlantic-origin storms. Severe storms affect the north-western coastal areas annually. Climate projections for Ireland indicate a modest decline in mean near-surface wind speeds of ~3 % annually, with summer reductions projected to decrease by up to 8 % by the end of the century (2071–2100) under high CO_2 emissions scenarios (SSP5-8.5), while winter wind energy is projected to remain relatively stable (Environmental Protection Agency, 2024). However, projected wind strength and storminess remain highly uncertain due to the limitations of current climate models in simulating large-scale atmospheric circulation patterns, including jet stream behaviour (Manning et al., 2023).

A recent paleostorm study (Sjöström, 2024), covering storminess variability over the last 8000 years in northwestern Ireland (Co. Mayo), showed that lower wind-strengths prevailed during the warmest part of the mid-Holocene, followed by increased wind strengths when northern

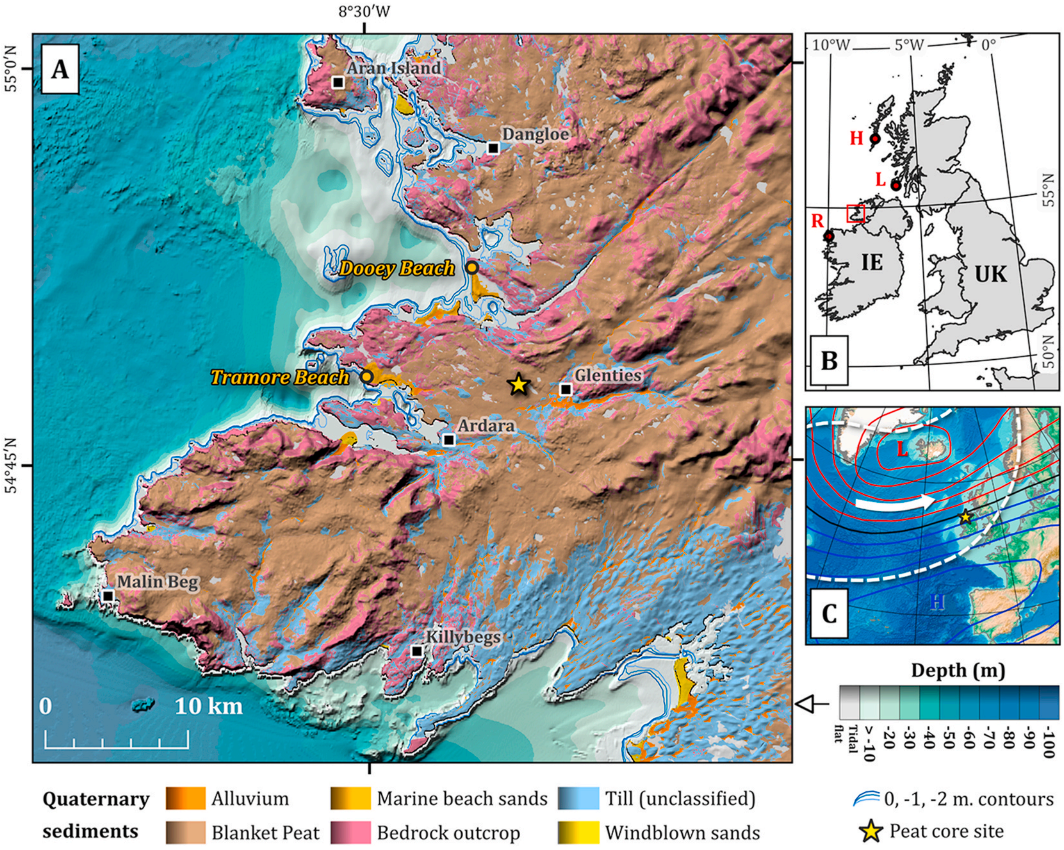

Fig. 1. A) Orientation map and quaternary geology map (GSI Quaternary sediments 1:50k, bathymetry (EMODnet, 2024), and hillshaded topography over the study area (EU-DEM, 2025). Peat coring location indicated by yellow star. Sea-level contours based on Kirby et al. (2023). B) Location map of the field area Ireland (IE) and the United Kingdom (UK), including location (red circle) of comparison sites (H=Hilltop Bog, Outer Hebrides, UK; L = Laphroaig Bog, Inner Hebrides, UK; R=Roycarter Bog, Co Mayo, IE). C) NAO and storm track of the NW Atlantic. The North Atlantic Oscillation (NAO) is shown by contours of the leading empirical orthogonal function (EOF) of winter (DJFM) sea level pressure anomalies (Hurrell et al., 2024) over the North Atlantic (20-80°N, 90°W-40°E). The white dashed line marks the average boundary of the storm track density (<980 hPa) computed for 7 different reanalysis datasets (Feser et al., 2021) for the extended winter (ONDJFM) seasons 1980–2015 over the North Atlantic area.

hemisphere temperatures started to decrease. In total 11 storm periods were recorded with two longer storm periods identified in the late mid-Holocene while shorter, and higher frequency (n = 9), of events were observed in the cooler late-Holocene. This suggests that the processes governing storminess over Ireleand shifted between the mid- and the late-Holocene. A comparison with paleostorm records from western Scotland (Orme et al., 2016; Kylander et al., 2020) showed a complex pattern of storminess with a mostlyantiphase relationship between 6500 and 3000 cal yr BP, followed by more variability and in-phase storminess periods from 3000 until the present. It remains unclear whether the complex storminess patterns observed across peatland records reflect real differences in storminess, or methodological and interpretational differences. In a recent study, Orme et al. (2026) found, based on analysis of two independent sources, namely a blanket bog record and historical written records, that increased storminess occurred following volcanic eruptions, linking increased storminess to volcanic activity.

This study contributes with an additional paleostorm record from north-western Ireland (Co. Donegal), using the same analytical approach as Sjöström et al. (2024), allowing a more direct comparison of hydro- and wind-climate over multimillennial timescales. The natural archive that will be targeted in this study is a blanket peatland. Blanket peatlands are only found in regions with high annual precipitation and cool annual temperatures (Gallego-Sala and Colin Prentice, 2013). Due to the hyperoceanic climate of northwestern Ireland, the landscape in coastal areas is blanketed by peat. Blanket peatlands also accumulate proxies of past environmental and climatic conditions, and have been used to reconstruct past vegetation, volcanic eruptions, hydrology, storm, temperature and wildfire variability (Blundell et al., 2008; Charman et al., 2009; Swindles et al., 2011; Orme et al., 2016; Kylander et al., 2020; Sjöström, 2024).

Here, the inorganic, mineral part of the peat matrix will be used to infer past wind strengths, together with analysis of the organic constituents of the peat to reconstruct the hydroclimatic conditions. This is conducted through coupling analysis of past peat accumulation rates, plant macrofossil content, and spectroscopic analysis of the organic constituents with grain size analysis of the mineral fraction of the peat matrix. Past fire incidence is reconstructed both through microscopic identification of charcoal particles, combined with FTIR spectroscopic analysis. By taking a multiproxy approach, past variability of hydro-, fire and wind-climate variability is reconstructed. We then compare regionally available storminess records from coastal bogs in Ireland and the UK to explore the climate processes affecting past hydro- and wind climate throughout the studied period.

2. Site description

The Glenties Bog (WGS84: 54°47.949′N, 8°20.048′W, 51 m.a.s.l.) is located in a coastal setting in County (Co) Donegal, northwestern Ireland (Fig. 1). The study site is located in a region with a cool and humid oceanic climate characterised by low seasonal temperature variability. The annual average temperature is *c.* 10 °C, with high annual precipitation (1100 mm yr^{-1}) and wind speeds (5.3 m s^{-1}) (annual averages 2011-2023 CE, Finner weather station, Met Éirann, 2024). During the winter months (Dec-Feb) temperatures are somewhat lower (6.3 °C) and wind speeds are strengthened (6.4 m s^{-1}). The highest gust winds generally occur during the winter months, and annually reaches above 33 m s^{-1} (annual averages 2011-2023, Finner weather station, Met Éirann, 2024).

The bedrock geology in the region consists of granites, quartzite, pelitic to semi-pelitic schists and sandstone together with the occurrence of amphibole-rich plutonics and metadolerite (Geological Survey of IrelandSpatial Resources, 2024). The Quaternary deposits in the study area are dominated by blanket peat together with localised occurrences of till, beach sediments, and estuarine silts and clays (Fig. 1).

3. Methods

3.1. *Sampling, bulk density and ash content*

The study site is located in an area dominated by blanked peat, near Glenties town (Fig. 1). Peat cores were retrieved with a Russian peat corer equipped with a 100 × 7.5 cm chamber. In total seven peat cores were retrieved from two alternating boreholes, with 25 cm overlap, reaching a vertical depth of 510 cm. The top 30 cm were not retrieved. pH was measured directly after core retrieval on the fresh peat surface (n = 9) using an ExStik pH analyser. Following core retrieval, the cores were put in split PVC tubes, wrapped in plastic, and stored at 4 °C after transport to Stockholm University. The current surface vegetation was also sampled (n = 1), by cutting a block of living vegetation (c. 20 × 30 cm) using a stainless-steel knife. The living vegetation block was put in a sample bag and stored at 4 °C at Stockholm University. The bulk density of the peat samples was calculated from the volume and dry weight of freeze-dried peat cubes of a defined size (2 cm^3, n = 481) following Givelet, 2004. The bulk density results were used to aid core correlation for the composite sequence of 481 cm. The ash residue, the inorganic residues left after combustion at 550 °C (Dean, 1974), was determined at 1 to 3 cm intervals (n = 231).

Sediment samples from local beaches were collected from Tramore Beach (54°48′17.91″N, 8°30′0.72″W) and Dooey Beach (54°52.393′N, 8°23.047′W), located 10 km west and 8.5 km north of the coring location respectively (Fig. 1). For the sediment sampling, the upper 10 cm of topsoil was removed and a c. 500 g sample was collected and stored in plastic bags.

3.2. *AMS radiocarbon dating and age-depth modelling*

Eight plant macrofossil samples were sent for AMS radiocarbon dating to the Tandem laboratory (n = 6), Uppsala University (Sweden) and Beta Analytics (n = 2), Miami (US) (Table 1). To avoid chronological uncertainties associated with using bulk peat samples for ^{14}C dating (Essell et al., 2025), only selected plant macrofossil remains were here used for ^{14}C dating and chronology building. The pretreatment includedsieving the bulk peat sample through a 500 μm standard sieve using distilled water. The above 500 μm reside was transferred to a Petri dish, where suitable macrofossils were picked out under a light microscope (10-40× magnification). Plant macrofossil identification was guided by Wohlfarth et al., 1998 , Mauquoy et al., 2010; Mauquoy and van Geel, 2007. Calibration and Bayesian age–depth modelling were conducted using the R package Bacon Blaauw and Christen, 2011, version 2.5, and the IntCal20 calibration curve (Reimer et al., 2020).

Table 1
Depth, laboratory identification reference, radiocarbon and calibrated ages.

Depth (cm)	Lab-id	Material used for dating	14C yr ±1σ	Calibrated age range, BP, 2σ
93	Ua-81508	Woody twigs	1117 ± 29	955–1175
137	Ua-81509	Woody twigs	1760 ± 29	1570-1710
225	Ua-81510	Sphagnum stems and leaves	2465 ± 29	2370–2710
289	Beta-621770	Sphagnum stems and leaves	3090 ± 30	3220–3375
378	Ua-81511	Eriophorum spp. Stems	3992 ± 29	4415–4520
418	Ua-81512	Woody charcoal	4779 ± 29	5475–5585
462	Ua-81513	Woody charcoal	5556 ± 33	6300–6395
499	Beta-622818	Woody heather remains. Carex seeds and stems.	6410 ± 30	7270–7420

3.3. Plant macrofossil analysis

To reconstruct the main changes in vegetation composition, plant (sub)macrofossils were examined throughout the sequence ($n = 31$). The plant macrofossils method followed Mauquoy et al. (2010) and Väliranta et al. (2007). Volumetric subsamples of 4-5 ml were gently rinsed in a 100-μm sieve under running water, and the residue was microscopically analysed for percentage proportions of main peat-forming plant components (total sample volume 100%). When the organic remains were unidentifiable, a percentage of unidentified organic material was determined. To visualise the plant macrofossil data, six functional vegetation groups were considered: monocots, Ericaceae, woody, *Sphagnum* mosses, other mosses and unidentified organic matter (UOM). Charred plant remains or charcoal < 1mm and >1 mm were counted as exact numbers. The counting was stopped if the number of charred remains exceeded 50.

3.4. FTIR-ATR analysis

Analysis of 165 finely milled bulk peat samples was performed by Fourier Transform Infrared Spectroscopy - Attenuated Total Reflectance (FTIR-ATR) using an Agilent Technologies Cary 630 equipment at the Department of Ecology and Geoscience, Umeå University (Sweden). In addition, the samples analysed for plant macrofossil content (Section 3.3, $n = 31$) were also analysed by FTIR-ATR (Agilent Technologies Cary 630) at EcoPast Laboratory, Universidade de Santiago de Compostela (Spain) to allow inter-methodological comparison. The analysis at both locations followed the same protocol; spectra were retrieved in the mid-infrared region (MIR, 4000–400 cm^{-1}) at a resolution of 4 cm^{-1} by averaging 200 scans per sample. Between samples, the equipment was thoroughly cleaned and a background measurement collected. The results were pre-processed in Orange data mining software (ver 3.37; Demsar et al., 2013): baseline correction, average and standard deviation spectra, and second derivative spectra. MIR ratios between selected wavelengths (Table 3) were plotted against time to explore the temporal variability of organic compounds. To explore associations between MIR ratios and plant macrofossil content, Pearson coefficients between the variables were also calculated ($n = 31$). The Pearson coefficients were calculated on standardised (z-scores) values of the results, as outlined in Section 3.5.

3.5. X-ray fluorescence (XRF) elemental analysis

A total of 165 bulk peat samples were milled and analysed for elemental composition in a Spectro XEPOS 3 Energy Dispersive X-ray fluorescence (ED-XRF) analyser. The equipment is hosted at the Department of Geography and Planning, Liverpool University (UK). The samples were hand pressed in 20 mm diameter pots and measured under a He atmosphere under combined Pd and Co excitation radiation and using a high-resolution, low spectral interference silicon drift detector. Daily standardisation procedures provide a system check on the XRF analyser, with accuracy verified using 18 certified reference materials (e.g. Boyle et al., 2015). Element concentrations derived by XRF were corrected for LOI in the onboard Spectro XEPOS 3 software, using LOI values calculated from ash content, with the results ultimately expressed as mass concentrations per unit dry mass (μg g-1 or mg g-1).

Concentration values for individual elements were calculated into mass accumulation rates (MAR) by multiplying the concentration value by the PAR ($g\ m^2\ yr^{-1}$). The results were then statistically assessed by PCA. Before the statistical analysis, the results were screened for outliers, zeros were removed, and the remaining results were converted to z-scores. By calculating the values to z-scores, the data are transformed to average-centred distributions, which avoids scaling effects (Eriksson et al., 1999). The z-scores were calculated as follows:

$$zi = (xi - \mu)/\sigma$$

Where zi represents the z-score, xi is the measured value at each data point (depth), μ represents the average value of each element, and σ represents one sigma standard deviation. Principal component analysis (PCA) was conducted using the JMP software (ver. 17), in correlation mode with a varimax rotation.

3.6. Grain size analysis: beach sediments and peat ash residues

Grain size analysis of the beach sediment samples ($n = 2$) was conducted on bulk samples following washing in distilled water and drying at 60 °C. Grain-size analysis of the downcore peat samples ($n=61$) and the surface sample ($n = 1$) was conducted on the ash residues obtained from the LOI procedure. To remove combustion residues (e.g., salts) and carbonates, the peat ash residues were soaked with 10% HCl, ultrasonicated for 30 s, and left to react for 2 h. Grain size distributions were measured using a Mastersizer 3000, equipped with a Hydro MV, allowing analysis of small sample volumes. The instrument employs a He-Ne red laser ($\lambda = 632.8$ nm) as well as a blue light LED ($\lambda = 470$ nm). The sample was added to the dispersion unit together with 0.6 ml of 3% $NaPO_3$ to facilitate particle disaggregation and left for 3 min prior to analysis. Measurements were repeated five times, capturing grain sizes ranging from 0.01 μm (clay) to 3500 μm (very coarse sand). The results are from the analysis are reported in 100 grain size bins, in volume % per grain size bin. From the five repeated measurements, an average was calculated, which was used for interpretation and statistical processing. Grain size classes are here descried according to Friedman and Sanders, 1978, and presented in ten categories (μm) that are organized based on the range of observed grain sizes: clay: 0-2 μm; very fine silt: 2-4 μm; fine silt: 4–8 μm; medium silt: 8–16 μm; coarse silt: 16–31 μm; very coarse silt: 31–63 μm; very fine sand 63–125 μm; fine sand: 125–250 μm; medium sand: 250–500 μm; coarse sand 500-1000 μm.

3.7. Powdered X-ray diffraction (pXRD) analysis

The beach sediment samples from Dooey ($n = 1$) and Tramore Beach ($n = 1$) were wet sieved into five size fractions: <63, 63-125, 125-250, 250-500, and >500 μm, using standard sieves followed by pXRD analysis to establish the mineral composition of the different grain size fractions. One bulk sample from each beach was also analysed by pXRD. From the peat sequence, the ash residues (LOI 550 °C) of five samples from the following depths: 36, 92, 231, 319, 398, and 431 cm, were analysed for mineral composition. The pre-treatment of the samples (beach sediments and peat ash residues) included washing in distilled water, drying at 60 °C and milling, using a pestle and mortar, to a fine powder (Sjöström et al., 2019). The peat ash residues were also washed in 10% HCl to remove combustion residues (e.g., salts). The samples were mounted on off-axis (zero background) silica plates.

pXRD analyses were conducted at the Swedish Museum of Natural History, Stockholm, using a PANalytical X–ray diffraction system (X'Pert^3 Powder) equipped with a multi-detector. The samples were analysed from 5° to 70° 2θ, with CuKα radiation ($\lambda = 1.5406$ Å) at 45 kV and 40 mA, passing through a curved graphite monochromator, fixed divergence and receiving slits (1°), step size 0.017° and a count time of 38 s. Processing of the diffractograms (background determination, smoothing, peak localisation and mineral identification) was done in HighScore 4.6, a PANalytical software (Degen et al., 2014) with integrated mineral reference patterns from the ICSD database (2012). Mineral identification was also guided by Brindley and Brown (1984) and Moore and Reynolds (1997). The Rietveld refinement method (Rietveld, 1969), which quantifies the relative occurrence of the mineral phases, was conducted using the HighScore default settings (Degen et al., 2014).

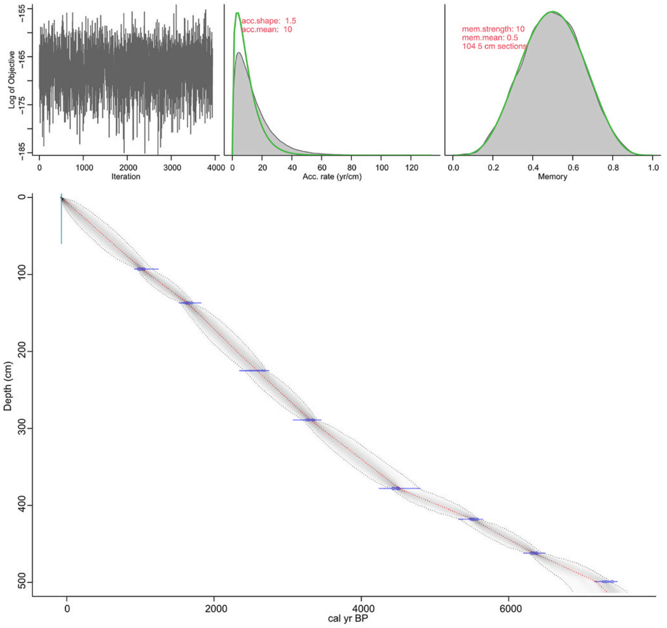

Fig. 2. Calibration and age-depth model of the peat sequence, constructed in R. Bacon ver 2.5 (Blaauw and Christen, 2011) using IntCal20 calibration curve (Reimer et al., 2020). Calibrated probability distributions of the nine ^{14}C dates are shown in blue. The red dotted line represents the weighted mean of the age-depth model, and the grey shading indicates the 95% confidence range. The three top boxes show information about the model, starting from the left: 1) quality of the iteration; 2) predicted (green line) accumulation rates versus actual mean (grey shape), and 3) memory values used in the a priori information in the Bayesian statistical approach (Blaauw and Christen, 2011).

4. Results

4.1. AMS radiocarbon dating and age-depth modelling

The result of the AMS radiocarbon dating showed that all the ages occur in stratigraphic order, with the lowermost sample showing the oldest age and decreasing ages towards the surface (Table 1, Fig. 2). The calibration and age-depth modelling (R.Bacon, Blaauw and Christen, 2011) show that the Glenties Bog sequence covers the last 7400 cal yr BP.

The acquired weighted mean ages and the accumulation rate (cm yr^{-1}), together with the bulk density, were used to calculate peat, ash and elemental mass accumulation rates (PAR, AAR and MAR, respectively), as well as to plot results on a calibrated years before present (cal yr BP) age scale.

4.2. Bulk density, peat accumulation rate, ash content, ash accumulation rate and pH

The minimum, maximum, average and standard deviation (2σ) values of the results described here are outlined in Table 2, and the variability through time is depicted in Fig. 3. Between 7230 and 5860 cal yr BP, higher bulk densities (average 144 mg cm^{-3}, n = 67) are observed compared to after 5860 cal yr BP (average 75 mg cm^{-3}, n = 414). The bulk density and PAR largely co-vary throughout the sequence, with a stronger agreement in the lowermost, denser part of the sequence (r^2 = 0.67, n = 67), compared to the uppermost part of the sequence (r^2 = 0.57, n = 414). Above average PAR (>58 g m^{-2} yr^{-1}) values are observed between: 7120-7075, 6850-6580, 6510-5960, 5620-5560, 4490-4475, 4450-4180, 4030-4000, 3810, 3375-3350, 3310, 3150, 2970, 2790, 2585-2555, 2320-2300, 2280-1610, 1210, 1110-1080, 1030-990, 995-770, and 730-455 cal yr BP. The ash content (%) and ash accumulation rate (AAR, g m^2 yr^{-1}) co-vary (r^2 = 0.86, n = 231) throughout the sequence, with above average values observed in the oldest part of the sequence (7230-5825 cal yr BP), followed by lower values. Thereafter, elevated values are observed at 3590, 2830, 2575, 1880, 1630, 1250-1040, 880, and from 660 cal yr BP towards the present. The pH gradually decreased from the lowermost to the uppermost measurement, varying from pH 5. (505 cm depth, 7080 cal yr BP) to 4.2 (40 cm, 280 cal yr BP).

Table 2
Summary results for peat properties and elemental data. A.) Peat properties values for pH, bulk density mg cm^{-3} (Bd), peat accumulation rate (PAR) g m^2 yr^{-1}, ash content (%) and ash accumulation rate (AAR) g m^2 yr^{-1}.

A. Peat properties	pH	Bd	PAR	Ash, %	AAR
Min	4.22	36	30	1.1	0.5
Max	5.30	197	116	10.6	6.0
Average	4.94	85	58	2.6	1.5
Sd (2σ)	-	59	26	2.6	1.9
Count	9	481	481	231	231

Table 3
Selected IR ratios and bands, their interpretation, and references.

ID	IR bands and ratios, cm^{-1}	Compounds and proxy indication	References
IR_pd	1600/1030	Aromatics/polysaccharides: Vegetation changes and/or peat decomposition.	(Artz et al., 2008; Broder et al., 2012; Biester et al., 2014)
IR_cb	(1705 + 1730)/ 1600	Carboxyl/aromatics: relative abundance of carbonyl versus aromatic compounds	(Broder et al., 2012; Hodgkins et al., 2014)
IR_ar	1600/ (2920 + 2950)	Aromatics/Aliphatic: vegetation change, decomposition or fires.	(Zaccone et al., 2014; Doskočil et al., 2016)

4.3. Plant macrofossil analysis

A simplified version of the main vegetation groups is presented in Fig. 3, while the full plant macrofossil results can be found in the Supplementary file (SFig. 1). During the first 2000 years of the record (c. 7100–5030 cal yr BP), the plant macrofossils are dominated by woody tree and monocot remains. The tree macrofossils include *Pinus* sp., *Betula* sp., and *Alnus* sp. Fern sporangia are also observed together with *Molinia caerulea*. Charcoal was also detected for this period. *Eriophorum vaginatum* is detected between 5520 and 4470 cal yr BP. *Calluna vulgaris* and *Erica tetralix* first appeared at 5030 cal yr BP and are abundantly present afterwards. *Sphagnum* remains are found throughout the record after 5900 cal yr BP, but with higher abundance starting from 3890 cal yr BP. *Sphagnum austinii* occurs with varying abundance, from 5 to 70 %, between 3890 and 2630 Cal BP (342–239 cm) together with monocots and Ericaceae. *Sphagnum papillosum* is present from 3270 cal yr BP onward. *Sphagnum austinii* disappeared approximately 2600 years ago, and after that, the peat record is dominated by monocots, Ericaceae and other *Sphagnum* species, together with periodic presence of non-Sphagnum bryophytes (S Fig. 1). Charred remains and charcoal particles <1 mm are detected throughout the peat sequence. Higher amounts (>50) of charred material >1 mm are observed at cal yr BP: 6700, 6270, 5920, 5030, 4270. Strongly burnt peat is observed at 6690 and 5030 cal yr BP.

4.4. FTIR-ATR analysis

The spectra of all the analysed samples and a description of the main absorbances and associated organic compounds can be found in the supporting information (SI result text and SFig. 2). The IR_pd ratio, reflecting changes in aromatics over polysaccharides (Table 3) stays above the average value (0.7) between 7260 and 5830, at 5730 and between 5670 and 4390 cal yr BP, followed by below average value

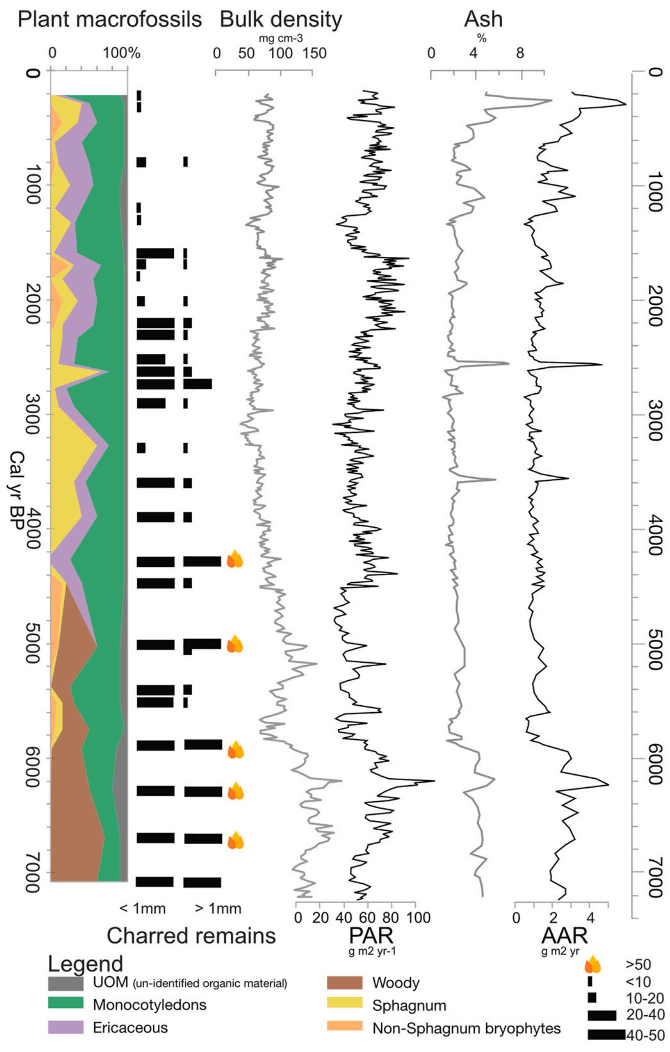

Fig. 3. Plant macrofossil content, charred remains, bulk density (mg cm^{-3}), peat accumulation (PAR, g m^2 yr^{-1}) ash content (%) and ash accumulation rate (AAR, g m^2 yr^{-1}).

towards the present (Fig. 4). IR_ar, reflecting aromatic over aliphatic compounds, is above the profile average (0.7) (cal yr BP): 7210-6850, 6710–6640, 6020-5900, 5790–5140, 4980–4580, 4470–4430, 3950, 3740–3650, 1840, 1775–1740, 1020, 870, and between 550 and 510 cal yr BP. The IR_cb ratio, representing carbonyl over aromatic compounds, stays above the profile average (0.9) at (cal yr BP): 7260–5960, 5690–5630, 5570–5510, 4650–4580, 4470, 4360–4240, 3410, 3340–3260, 3165, 2820, 2500, 690–580, 440–300, and 220 cal yr BP.

4.5. *Linking charcoal remains to FTIR ratios*

The correlation analysis, conducted between the standardised results of the plant macrofossil analysis and the FTIR ratios, shows that a strong correlation (>0.7) is displayed between woody remains, charred remains and IR_pd (STable 2). A weak to moderate positive correlation (0.3–0.69) is displayed between UOM (unidentified organic matter), woody remains, charred remains, IR_pd and IR_cb. Both ericaceous and sphagnum remains display a negative moderate to weak correlation with a majority of the compared variables.

Previous studies have shown that peat combustion causes a loss of easily degradable polysaccharides and a relative enrichment of recalcitrant aromatics and nitrogen compounds (Zaccone et al., 2014; Uhelski et al., 2022). As such, ratios involving these compounds may, in addition to reflecting microbial peat decomposition or vegetation composition, also change with past fire events and fire intensity (Artz et al., 2008; Biester et al., 2014; Martínez Cortizas et al., 2021; Constantine et al., 2021). Increases in the IR_ar ratio reflect relative increases of aromatic over aliphatic compounds, while IR_cb depicts changes in carbonyl content over aromatics. During a peatland fire, the organic matter undergoes distinct changes depending on the source vegetation and intensity of the fire. Fires of temperatures below 400 °C produce an increase of aliphatic and carbonyl compounds (Constantine et al., 2021), while fires with higher temperatures (>400 °C) are associated with a decrease in these two compounds, leading to a relative enrichment of aromatics (Constantine et al., 2021; Gao et al., 2022). For the Glenties record, this means that these ratios, during periods of peatland fires, may contain information about fire intensity. Higher IR_ar (lower IR_cb) values indicate higher fire intensities. The strong correlation (>0.7) between woody remains, charcoal (>1 and < 1 mm) and IR_pd (S Table 2), show that 1) fires are reflected also in the spectral data and 2) that fires were the main cause of the elevated decomposition in the oldest, lowermost, part of the Glenties sequence.

4.6. *XRF analysis*

Based on analytical performance and relevance to the study objectives, 16 elemental MARs were selected from the ED-XRF dataset (Al, Br, Ca, Cl, Fe, Ga, K, Mn, P, Rb, S, Si, Sr, Ti, Y, Zr; SFig. 3). A principal component analysis (PCA) including these elements together with PAR, bulk density (Bd), and AAR was performed to explore relationships between elemental fluxes and peat properties.

Five principal components ($_{XRF}$Cp1–$_{XRF}$Cp5) explain 92 % of the total variance (Table 4). $_{XRF}$Cp1 (41 %) is dominated by Al, Fe, Mn, Y, Bd, Sr, Ga, P, and Ti (loadings >0.7), with moderate contributions from Ca, AAR, S, and Cl. $_{XRF}$Cp2 (29 %) is associated with Zr, Si, K, Rb, and Br, with moderate loadings of AAR, Ca, Ga, P, and Y. $_{XRF}$Cp3 (9 %) is mainly

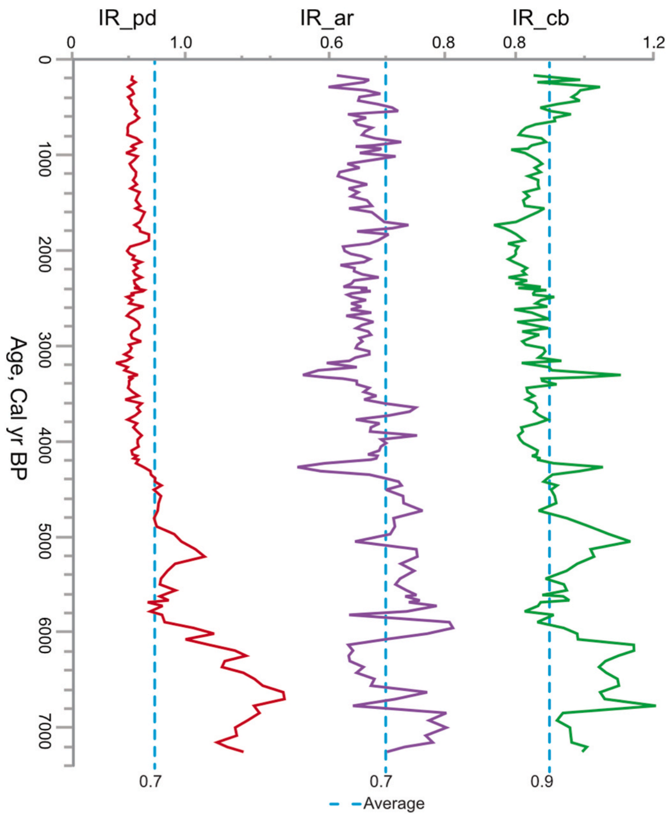

Fig. 4. IR ratios plotted against time. IR_pd: peat decomposition (aromatics over polysaccharides); IR_ar: aromatic over aliphatic compounds; IR_cb: carboxylic compounds over aromatics.

defined by S, with secondary associations of Ca and Sr. $_{\mathrm{XRF}}$Cp4 (7 %) and $_{\mathrm{XRF}}$Cp5 (6 %) are dominated by PAR and Cl, respectively.

Temporal variations in component scores highlight changing geochemical regimes through the sequence (Fig. 5). $_{\mathrm{XRF}}$Cp1 shows enrichment in the lowermost (oldest) peat, with secondary peaks at ~5730–5570, 5550–4510, 3740, and 330–220 cal yr BP. $_{\mathrm{XRF}}$Cp2 displays peaks ~6310–6250 and 6020 cal yr BP, followed by recurrent positive excursions at 3610, 2600, 1900, 1610, 1270–1060, 950, 910, and 650–180 cal yr BP, with a maximum near 300 cal yr BP. $_{\mathrm{XRF}}$Cp3 declines from 7260 to 6250 cal yr BP and exhibits positive phases around 5630, 4430–4000, 3410, 2820–2720, 2630–2600, and 2440 cal yr BP, and again between 2360–1710 and 1270–370 cal yr BP. $_{\mathrm{XRF}}$Cp4 shows recurring positive intervals from 7260 cal yr BP onward, particularly during 4510–4280, 2790–2690, 2260–1540, and 1100–370 cal yr BP. $_{\mathrm{XRF}}$Cp5 exhibits marked peaks (>0.7) between 6430 and 6080, 5040–4980, 2790–2630, 2390–2290, 1900–1610, 910, and 690–580 cal yr BP.

4.7. *Grain size analysis*

The beach sediment samples from Dooey and Tramore Beaches consist of well-sorted, unimodal fine sand with a modal grain size of 198 μm (SFig. 4). In total, 61 peat-ash samples were analysed for grain-size distribution. Most samples are poorly to very poorly sorted, showing bi- (n = 35) or polymodal (n = 20) frequency distributions, while six samples exhibit unimodal curves (Fig. 6). Between 5540 and 1275 cal yr BP, the median grain size (Dx50) lies within the coarse-silt fraction (mean = 25 μm, n = 41), increasing to fine sand (mean = 76 μm, n = 5) between 1160 and 370 cal yr BP, before returning to coarse silt (mean = 17 μm, n = 6) from 370 cal yr BP to the present.

Fig. 7 shows the temporal distribution of grain-size fractions from clay (<2 μm) to coarse sand (500–1000 μm), alongside the results of hierarchical cluster analysis (four clusters). Clusters 1–4 represent progressively higher proportions of coarse grains. As entrainment of sand-sized particles (>63 μm) requires stronger winds (Vandenberghe, 2013), clusters 3 and 4 are interpreted as indicators of increased wind energy and storm activity. Samples assigned to cluster 4 (highest sand content) define four distinct storm periods: SP1 = 3415, SP2 = 1160–1080, SP3 = 910–750, and SP4 = 620–370 cal yr BP.

4.8. *pXRD analysis*

The mineral composition of the peat samples (n = 7) is dominated by quartz, plagioclase (mainly albite) and K-feldspar together with the occurrence of micas (biotite and annite) (STable 3). Higher (>50%) quartz content occurs at 4750, 2540, 890, and 230 cal yr BP, with the highest occurrence noted at 890 cal yr BP (70%). The mineral composition of the source sample from Dooey Beach consists of quartz, albite, K-feldspar, calcite, dolomite, aragonite, mica (biotite, annite, muscovite), chlorite, hornblende and birnessite (Table 4). The Rietveld quantification showed that quartz dominates (75%) the composition of the bulk sample. For the size fractionated samples, a trend of increasing quartz content from the finer fractions (<63) towards fine sand (125-250 μm) is observed, mirrored by a higher K-feldspar and chlorite with decreasing grain size. Above 250 μm, carbonates (calcite and aragonite) dominate (>90%), likely from shell fragments (inferred from visual observation). The mineral composition of Tramore Beach follows a similar trend as that of Dooey Beach, but with a lower content of carbonates (20%) in the 250-500 μm size fraction (S.Table 4). The quartz content is also higher (90%) in the bulk sample.

4.9. *Linking the chemical, mineral and grain size results*

Based on the focus of this study, emphasis will here be put on comparing elemental variability ($_{\mathrm{XRF}}$CP1 and $_{\mathrm{XRF}}$Cp2) and relating these to the observed mineral and grain size compositions.

Table 4

Results of the PCA analysis of elemental mass accumulation rates, bulk density (bd), ash and peat accumulation rates (AAR, PAR).

Variable	$_{\mathrm{XRF}}$Cp1	$_{\mathrm{XRF}}$Cp2	$_{\mathrm{XRF}}$Cp3	$_{\mathrm{XRF}}$Cp4	$_{\mathrm{XRF}}$Cp5
Expl. Var.%	41%	29%	9%	7%	6%
Cumul.var.%	41%	69%	78%	86%	92%
Al	**0.95**	0.03	0.14	0.05	0.16
Fe	**0.94**	0.18	0.23	0.05	0.03
Mn	**0.93**	0.19	0.20	0.07	0.14
Y	**0.89**	0.33	0.22	0.07	0.13
Bd	**0.88**	−0.06	−0.07	0.34	0.07
Sr	**0.84**	0.20	0.43	0.08	0.14
Ga	**0.76**	0.56	0.08	0.08	0.07
P	**0.71**	0.35	0.01	0.18	0.33
Ti	**0.71**	0.49	0.05	0.16	0.26
Ca	0.68	0.11	0.61	0.16	0.24
Zr	0.17	**0.96**	0.01	0.06	0.03
Si	0.22	**0.95**	−0.06	0.05	0.04
K	0.21	**0.93**	0.01	0.05	0.01
Rb	0.19	**0.87**	0.14	0.09	0.22
Br	−0.10	**0.84**	0.25	0.22	0.15
AAR	0.52	0.56	0.05	0.52	−0.08
S	0.32	0.07	**0.90**	0.17	0.04
PAR	0.18	0.21	0.23	**0.89**	0.18
Cl	0.44	0.23	0.13	0.18	**0.82**

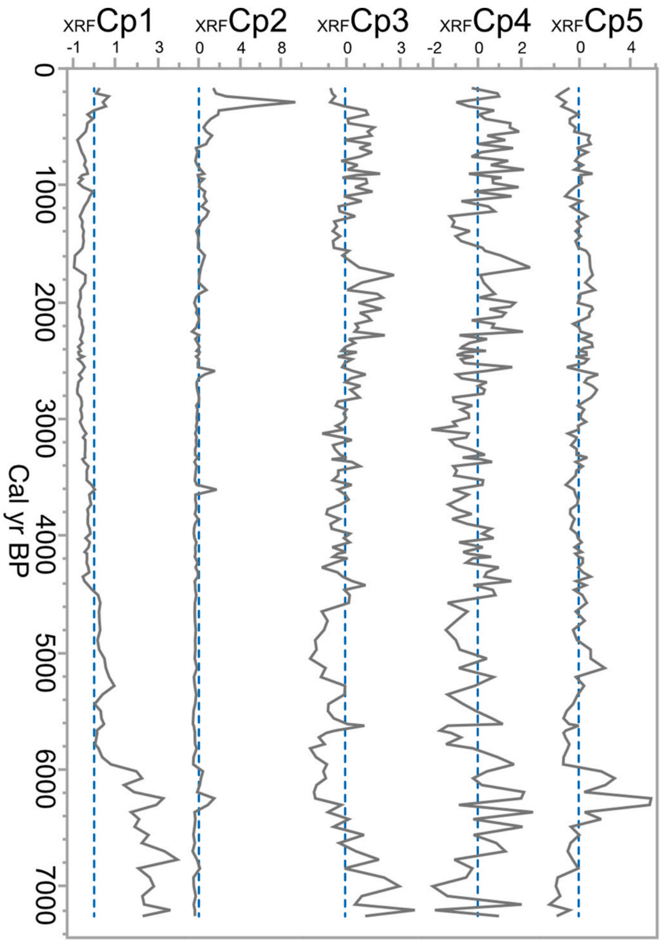

Fig. 5. $_{\mathrm{XRF}}$Cp1-5 plotted against time. The average of each factor is indicated by the blue dotted line. The individual elemental MAR values are depicted in SFig. 3.

Elements associated with $_{\mathrm{XRF}}$Cp1 represent the main variability of both the lithogenic (e.g. Al, Ti, Y) (Steinmann and Shotyk, 1997; Aubert et al., 2006) and soluble (Ca, Fe, Sr) phases in peat. Aluminium, Ti and Y are established proxies of fine mineral dust in peat records (Shotyk et al., 2002; Martínez Cortizas et al., 2005; Kylander et al., 2016), indicating that the period between c. 7200 and 5400 cal yr BP was dominated by fine-grained particles. The elements associated with soluble phases (Ca, Sr, Fe) are often enriched in the lowermost parts of peat deposits, both through upwards diffusion from underlying sediments (Steinmann and Shotyk, 1997) as well as dissolution, and downward migration, of mineral phases that are dissolved in the acidic peat (e.g., carbonates, phosphates and amphiboles) (Malmer, 1988; Le Roux et al., 2006; Sjöström et al., 2022). Furthermore, $_{XRF}$Cp1 also captures most of the variance in the bulk density (BD), which reflects the higher decomposition in the oldest and lower part of the record. The component also captures some of the variance of AAR, likely reflecting the fact that the ash residue contains a mixture of lithogenic, soluble and authigenic phases (Steinmann and Shotyk, 1997; Sjöström et al., 2022). Taken together, the first component captures the variance of the elements and peat properties that are highly enriched in the lowermost part of the sequence (Fig. 5), likely representing a mix of detrital, fine-grained minerals, soluble phases and elevated decomposition (higher bulk density values). No grain size data were acquired for this phase, due to the presence of highly resistant (e.g. charcoal) OM.

The second component, $_{XRF}$Cp2, captured 29% of the variance, and strongly associated elements Zr, Si and K, which are associated with lithogenic detrital minerals in peat deposits (e.g., Shotyk et al., 2002; Martínez Cortizas et al., 2005; Kylander et al., 2016). Silicon is the dominant element in silicate minerals but can also be associated with tephra shards and biogenic phases (phytoliths, diatoms). Here, Si is strongly associated with lithogenic elements, suggesting that its variance is mainly associated with detrital mineral input. Rubidium and Br are also strongly correlated to $_{XRF}$CP2. Rubidium may occur as a trace element in K-feldspars and micas (Nesse, 2017), both identified in the peat mineral matrix (S.Table 3), while Br is a halogen that may be associated with sea spray in peat deposits (Orme et al., 2015) that, following deposition, co-vary with OM decomposition processes (Bindler, 2006; Martínez Cortizas et al., 2016, 2025; Moreno et al., 2020).

Between 7260 and 2500 cal yr BP, three peaks in $_{XRF}$Cp2 are observed, at 6310–6080, 3610, and 2600 cal yr BP (Fig. 5), followed by a general increase and larger variability towards the present. From 2500 cal yr BP, the generally increasing trend is marked by episodic peaks at 1900, 1710, 1270–1100, 990–940, 650–620, and 400–175 cal yr BP, with the largest peak centred at 300 cal yr BP. When comparing the grain size distribution and $_{XRF}$Cp2, we note that periods of coarsening grain size distributions do not co-vary with increased lithogenic input.

Previous studies have used elemental ratio variations to infer changes in mineral composition and/or grain size in peat sequences (e.g., Shotyk et al., 2002; Kylander et al., 2013; Sjöström et al., 2022), but to decipher what the variability between two elements is reflecting it is recommended to anchor ratios with mineral and/or grain size analysis (Sjöström et al., 2019, 2020). For the Glenties sequence, ratios between Ti/Si and Al/Si (S Fig. 3) show higher values in the lowermost and oldest part of the sequence, reflecting higher Ti and Al input during this period, but show limited variability thereafter. The Ti/Zr is also elevated in the lowermost part, followed by less variability thereafter, but peaks generally co-occur with deposition of finer grain sizes, indicating that Ti is enriched in the finer grain sizes also at this study site. This is also confirmed by the pXRD analysis, where Ti-bearing mica and chlorite minerals are enriched during periods of finer grain size distributions in the peat, and in the finer size fractions of the beach sediments (section 4.7). This indicates that the Ti/Zr ratio mainly reflects grain size

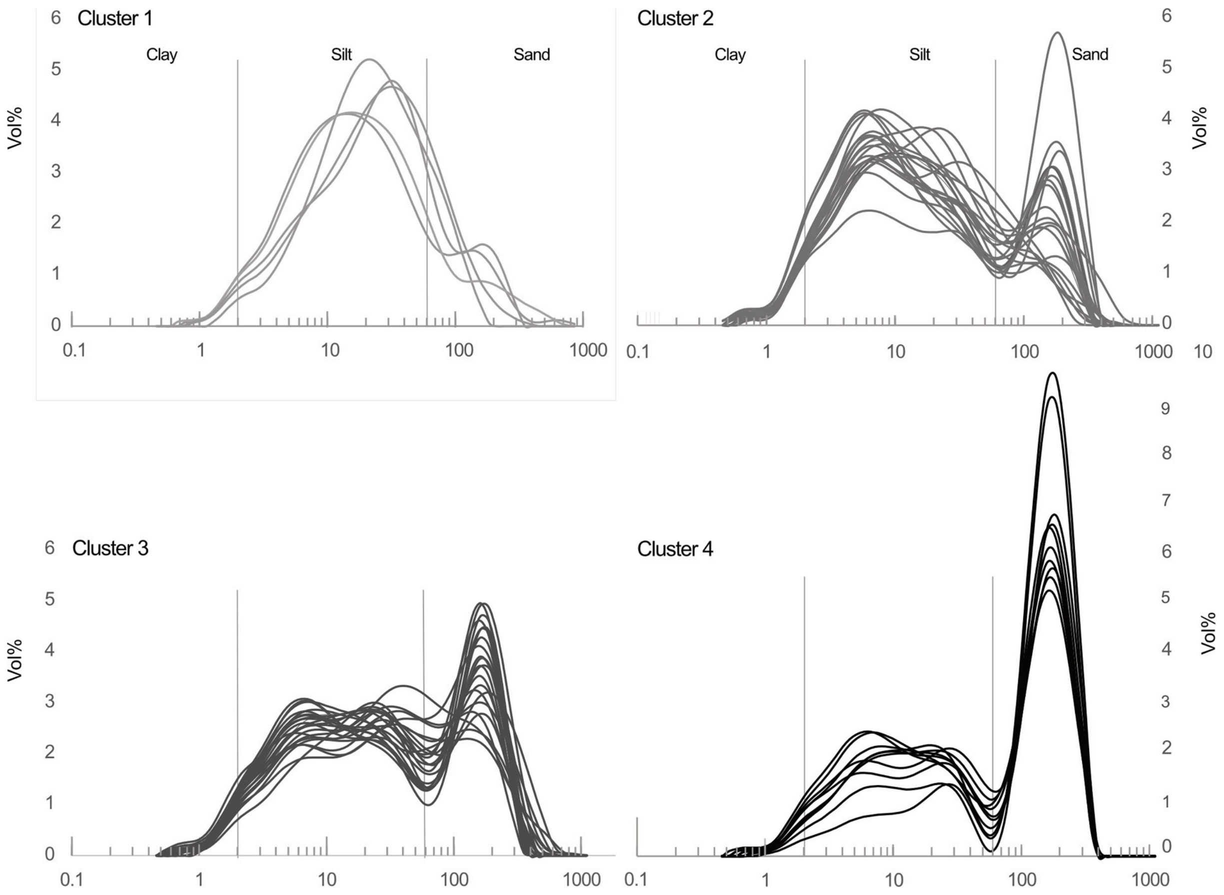

Fig. 6. Frequency curves and summary statistics of the grain size results, Glenties peat sequence. The frequency curves are grouped into four clusters, based on similarity of grain size distributions.

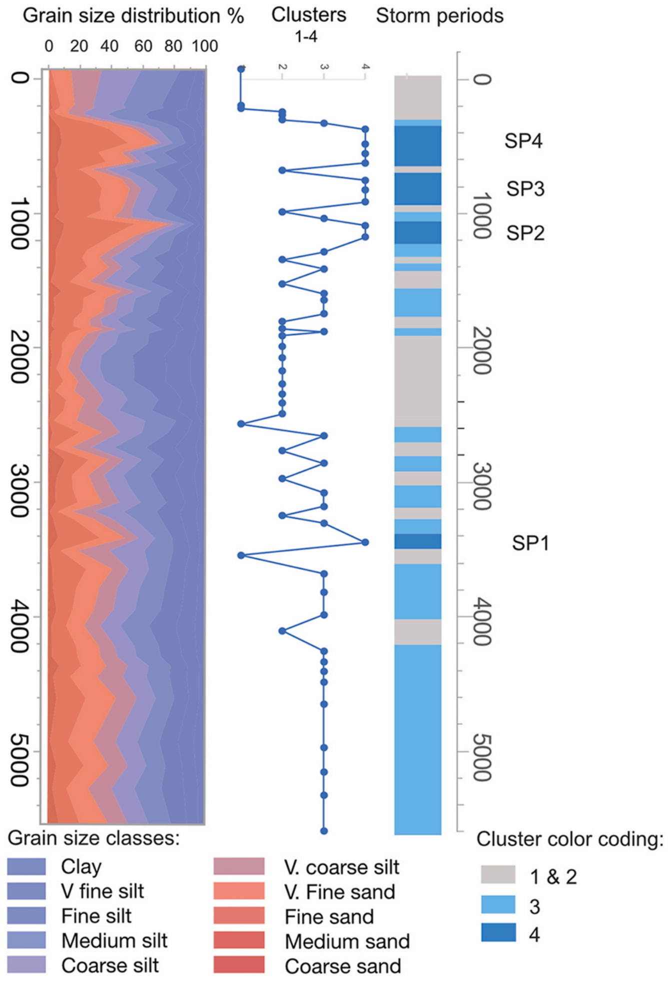

Fig. 7. Grain size distribution (%), clusters (1-4) and storm periods against time.

variability in the Glenties Bog sequence.

When comparing the results of the grain size analysis and the mineral composition of the source beach sediments to the peat mineral matrix, the latter seems to derive partly from other sources, based on an overall finer grain size distribution (Fig. 7, S.Fig. 4), and a distinct mineral composition compared to the beach sediments (S.Table 3, S.Table 4).

5. Discussion

5.1. Peatland development

The development of Glenties Bog is here presented in five phases (I-V) based on plant macrofossil content, bulk density, AAR and IR ratios (Fig. 8).

In Period I, 7230 – 5880 cal yr BP, woody vegetation (trees) and monocots co-occurred with intense fires, indicative of low water tables and relatively dry conditions. The bulk density and AAR were higher compared to later periods, likely representing a combination of compaction and loss of labile organic compounds during fires and a higher content of soluble phases (e.g. Ca, Sr, S Fig. 3) (SFigs. 3 and 8). The fire intensity was intense between 7230 and 6850 cal yr BP, and at 6635 cal yr BP (IR_ar ratio, IR_cb, Fig. 8). During Period II, 5880–4270 cal yr BP, woody vegetation and fires still occurred but at lower frequency and/or intensity. *Sphagnum* mosses appeared during period II. Taken together, this indicates that overall wetter conditions prevailed compared to period I. This general trend of increasing wetness was interrupted by a two fire episodes *c.* 5960–5900 cal yr BP and 5300 cal yr BP. This was followed by a steady rise in sedges, peaking at 4270 cal yr BP, coinciding with a fire event. During Period III, 4270 until 3000 cal yr BP, relatively wet conditions prevailed as evidenced by low fire incidence and high *Sphagnum* moss occurrence. Within period III, *Sphagnum* steadily increased until it dominated the assemblage at 3280 cal yr BP, after which it declined. The AAR was mostly low, except for an episodic increase at 3580 cal yr BP. This episodic increase in AAR is likely caused by crypto-tephra input; supported by visual inspection of the ash residue and identification of tephra shards. Period IV, 3000–1700 cal yr BP, was generally dominated by sedges and a return to increased fire incidence, indicating a return to drier conditions. An episodic increase in *Sphagnum* mosses was observed at 2630 cal yr BP. From 2230 until 1700 cal yr BP, an increase in partially decomposed non-*Sphagnum* mosses, heathers, and fires co-occurred, indicating that relatively dry conditions prevailed, together with recurring fire episodes. In Period V, 1590–220 cal yr BP sedges generally dominated the vegetation composition, and less fire activity was observed. Within the period, higher *Sphagnum* occurrence was observed around 1330, 1000, and 455–290 cal yr BP. Based on the low fire incidence and vegetation composition, this phase appears to have been relatively wet.

Based on a combination of the geographical location of the study site, the plant macrofossil content and low bulk density, pH and AAR content, the Glenties Bog displays the characteristics of an ombrotrophic (rain-fed) blanket bog. The alternating shifts between periods of higher and lower fire were recorded both in the plant macrofossil data and the IR ratios (STable 1 Fig. 8). Between 7230 and 4980 cal yr BP, woody vegetation, charcoal and higher decomposition were recorded (Fig. 8), indicating that dry conditions with recurrent fire episodes prevailed. From 4270 cal yr BP, co-occurring with the transition from the mid-to the late Holocene, a baseline shift is noted in both the vegetation composition (decreased woody occurrence, and increased *Sphagnum* presence) and lower fire incidence. This indicates that overall wetter conditions prevailed in the late Holocene compared to the mid-Holocene.

5.2. Links between fires, hydroclimate and storminess

Here, the relationship between past variability in fires (based on IR_ar, IR_cb and charcoal), hydroclimate (IR_pd, plant macrofossil content) and wind climate (grain size and chemical composition) results will be explored to evaluate the links between hydro- and wind climate through time (Fig. 8). Because relative sea level (RSL) changes may impact both sediment source areas and particle transport to coastal bogs we will here explore the grain size distribution at Glenties Bog against reconstructed RSL variability. RSL changes in Ireland are often complex, spatially variable and many areas suffer from data paucity (Kirby et al., 2023). For Donegal, the Bracky Bridge RSL curve (Kirby et al., 2023) is based on well-dated, high resolution diatom samples from a site only 7 km SW of our study site. This reconstruction indicates a steady relative sea level rise of about 1.8 m since 2.5 ka (Kirby et al., 2023, Fig. 8). This is in line with, but a slightly larger rise than, the model results of (Kuchar et al., 2012); however, it is incompatible with the Mid-Holocene high stand indicated by previous RSL curves based on GIA modelling (Shennan, 2018) which instead would suggest a gradual RSL lowering of about 1 m during the last 7 ka. Although the changing RSL affected the position of beach sediment sources (Fig. 1) it seems unlikely that these changes affected the grain size distributions at Glenties Bog to any great extent, since changes in the grain size distributions occurred episodically while the RSL changed gradually Furthermore, the rising RSL is not coupled with a general increase in either inorganic ash content, nor coarsening grain sizes. In addition, the grain size distribution at Glenties Bog is mainly dominated by finer grain sizes than the beach sediments (except for storm period II, III and IV), indicating that mainly other areas, and possibly more long distant sources, provided the bulk of the minerals deposited at Glenties Bog. Varying grain size distributions will therefore hereafter be interpreted as mainly a function of changing wind

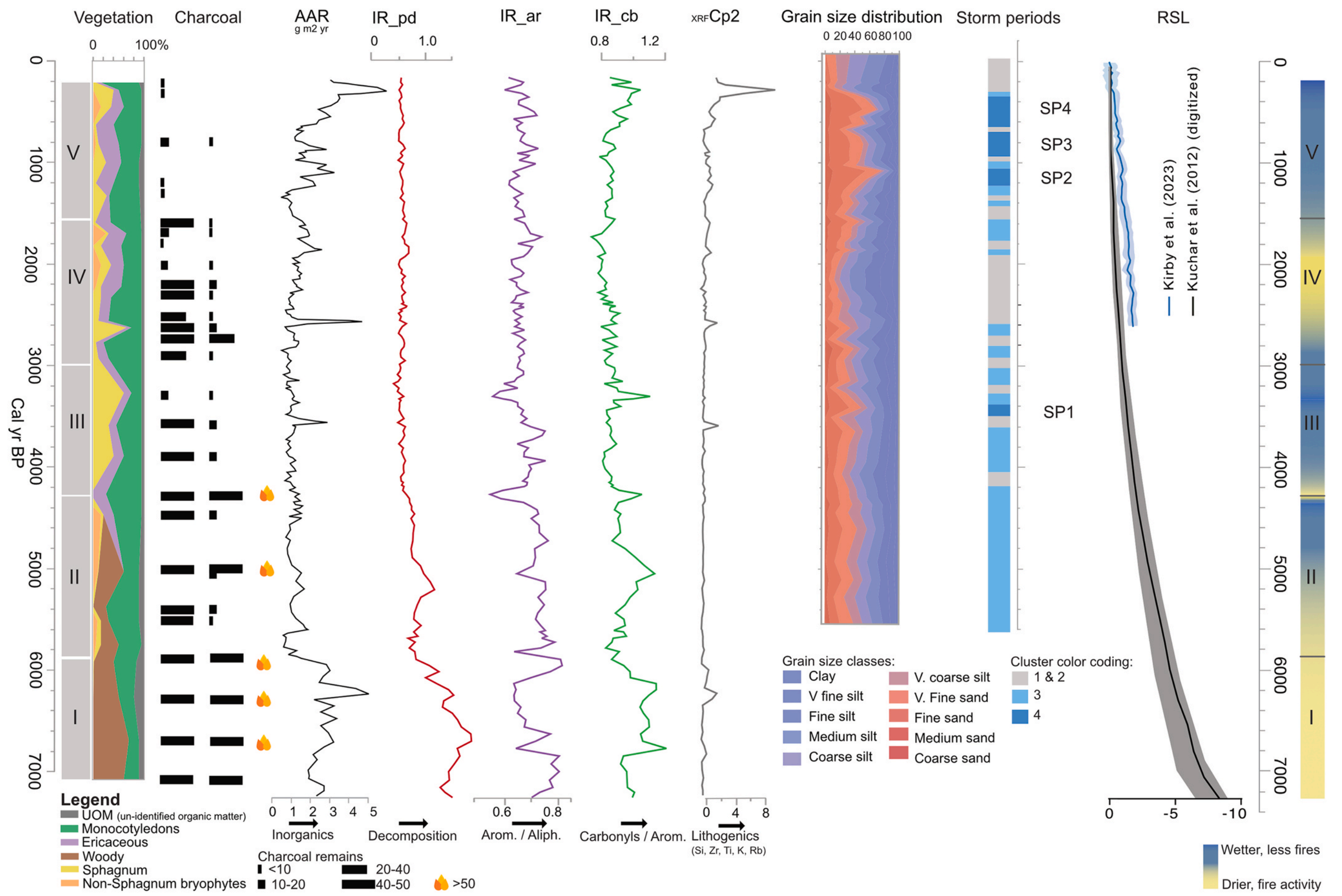

Fig. 8. Summary figure of selected proxies for the Glenties Bog sequence: plant macrofossil content, fire incidence (charred remains), AAR, spectroscopic ratios (IR_pd, IR_ar and IR_cb), $_{XRF}$CP2 depicting variability of lithogenic elements throughout the profile, grain size distribution and the result of the cluster analysis and inferred storm periods. RSL variability from Kirby et al. (2023) and Kuchar et al. (2012). Furthest right: a blue-yellow colour gradient representing the main hydroclimate and fire indications throughout the study period (I = dry and recurring fires; II = relatively dry but increasingly wet, fire occurrence; III = wet and less fires; IV = drier and fire occurrence; V = wet and minimal fire occurrence).

speeds.

Because stronger winds are required for aeolian entrainment and transport of particles (Pye, 1987; Vandenberghe, 2013), the results of the grain-size cluster analysis will here be used to infer past wind strengths, following the approach developed by Sjöström et al. (2024). Samples belonging to clusters 1 and 2 are interpreted as representing lower wind strengths (dominated by clay- and silt-sized particles), cluster 3 as reflecting intermediate wind strengths, and cluster 4 as indicating periods of increased wind strength and storminess (sand content 4–12%).

Period I stands out as the driest interval and the most affected by fires across the record. During this phase, the presence of highly resistant OM prevented laser grain size analysis, but the chemical composition (higher Ti and Al content) suggests that finer particles (S Figs. 3 and 8), and thus lower wind strengths, dominated throughout the period. The presence of trees in the peatland during this period further supports the interpretation that relatively dry conditions prevailed (e.g. Lieffers and MacDonald, 1989; Torbenson et al., 2015). Tree presence also indicates a less open landscape, which may have influence aeolian transport. During Period II (5880–4270 cal yr BP), increasingly wet conditions were inferred, with fires still occurring, but at a lower intensity compared to Period I. The grain size results (available from 5450 cal yr BP) indicate that relatively stable wind conditions prevailed. The start of Period III coincided with the Hekla-4 eruption, dated to ~4260 cal yr BP (Larsen and Þórarinsson, 1977; Pilcher et al., 1996; Wastegård, 2005), and the transition to the late Holocene (Walker et al., 2019). The Hekla 4 eruption coincided with intense fires and deposition of fine particles at Glenties Bog, indicating seasonally dry conditions and lowered wind speeds. Immediately after this event, coarser particles were deposited and overall wetter conditions were inferred (low fire incidence, increasing *Sphagnum* content), indicating a return to increased wind strengths and wetter conditions. Around 3600 cal yr BP, fires were again recorded, contemporary with an episodic increase in AAR and a finer grain size distribution, indicating a return to somewhat drier conditions and lower wind speeds. From visual inspection, it was noted that the AAR peak at 3580 cal yr BP was dominated by tephra shards, indicating that this AAR peak is related to a volcanic eruption. Immediately following this period, we again note increased wind strengths and the occurrence of the first storm period (SP1), recorded at 3415 cal yr BP. SP1 co-occurred with low fire incidence and wetter conditions (high *Sphagnum* content). Cool conditions and elevated volcanism has been reconstructed from ice core assemblages encompassing SP1 (Sigl et al., 2021, Fig. 9). The *Sphagnum* content peaked at 3275 cal yr BP, followed by a decrease in wetness and lower wind strengths (finer grain sizes) until *c.* 3200 cal yr BP. Somewhat wetter conditions are noted again thereafter. During phase IV, a return to more fires and overall drier conditions between c. 2700–2230 cal yr BP is paired with lowered wind strengths. From 2230 cal yr BP, fire incidence decreased. From 1900 cal yr BP, somewhat higher wind strengths (coarser particles) were inferred again.

In Period V, fire incidence dropped to a minimum while elevated AAR were recorded along with three storm periods: 1160-1080 (SP2), 910-750 (SP3) and 620-370 (SP4) cal yr BP. This shift overlaps with regional vegetation change and a marked decrease of trees as inferred from pollen records (Fossit, 1994), which may also have affected aeolian particle transport. In addition, this period was also associated with increased volcanic activity on Iceland, based on observations of crypto-tephra particles in north European lakes and bogs (Swindles et al., 2011; Sigl et al., 2021). Volcanic activity and crypto-tephra may also have contributed to some of the AAR peaks observed at Glenties, with peaks matching Hekla-1104 (850 cal yr BP); Hekla-1510 (440 cal yr BP) and Hekla-1693 (260 cal yr BP) (Larsen et al., 1999; Swindles et al., 2011). A marked decrease in the grain size is observed from 300 cal yr BP, contemporary with the largest AAR peak. This could reflect the overall lowering of the wind strengths in the region, fine-grained crypto-tephra affecting the grain size distribution, or be an effect of increased human activities such as agriculture, grazing, infrastructure projects (e.g., roads) promoting increased dust emissions (Silva-Sánchez et al., 2014; Hooper, 2018). Taken together, the proxies from Glenties Bog show an interplay between fire activity, hydro- and wind climate during the studied period, with increasing wind strengths and storminess associated with wetter conditions and less fires. For Glenties Bog, all four storm periods occurred directly following, or during, periods of increased volcanic activity, indicating that volcanism may have been an important forcing factor for regional storminess.

Fire activity, as recorded from charcoal particles and FTIR ratios, varied throughout the sequence, with overall less fire activity recorded in the cooler and wetter late Holocene compared to the warmer mid-Holocene (Figs. 8 and 9). These results indicate that the peat itself, and in particular fire activity, may also be an important indicator of hydroclimatic variability, and by extension of atmospheric circulation variability in the eastern North Atlantic.

5.3. Comparison with previous storminess records

The inferred wind and hydroclimate variability from Glenties Bog are here compared with palaeostorm records from coastal areas in Ireland and Scotland (UK; Fig. 9). The selected records are coastal peat bog sequences in which aeolian-transported particles serve as proxies for storminess. Particular emphasis is placed on comparison with the Roycarter Bog record (Co. Mayo, Ireland), located ~130 km southwest of Glenties Bog and analysed using the same proxy indicators and chronological framework (Sjöström et al., 2024) as applied here. The Scottish palaeostorm records included here employ somewhat different analytical approaches, and storm inferences are therefore not based on the same criteria. Hydroclimatic comparisons are restricted to the Irish sites.

The Roycarter Bog record shows overall coarser grain sizes (fine sand), a greater number of storm periods (11), and higher hydroclimatic variability compared with Glenties Bog. The grain size distribution at Glenties Bog is dominated by coarse silt, except between 1175 and 370 cal yr BP when fine sand prevailed, with in total four storm periods identified throughout the study period. Three of these (SP1, SP2, SP4) coincide with storm phases previously reported in Ireland (Sjöström et al., 2024; Orme et al., 2026), indicating that these periods represents phases of increased storminess for north-western Ireland. SP2 also overlaps with storm periods in the Inner Hebrides, while SP4 corresponds to storm events recorded at all four sites (Co. Mayo, Co. Donegal,

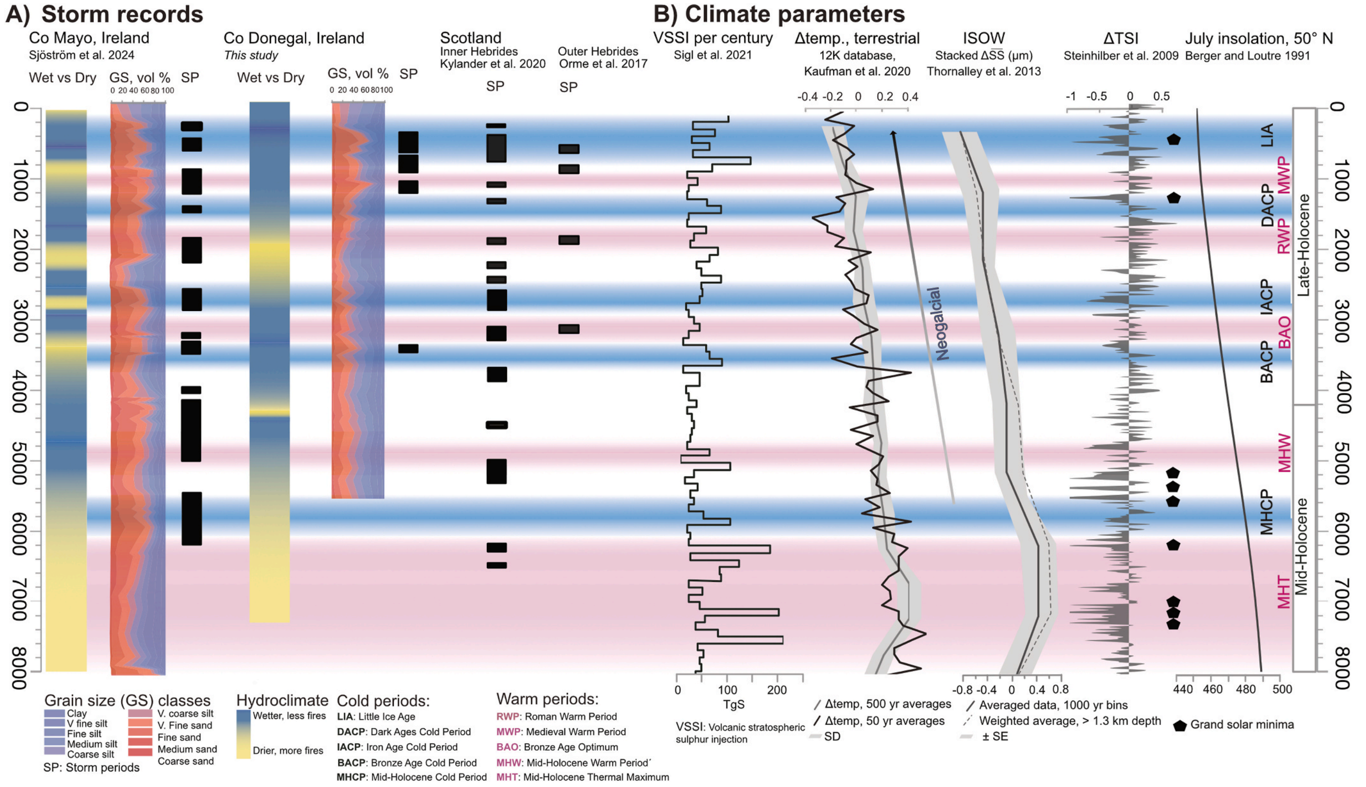

Fig. 9. Paleostorm comparison and climate parameters. A) The four paleostorm records arranged according to their geographical location: Co. Mayo (Sjöström et al., 2024), Co. Donegal (this study) Inner Hebrides (Kylander et al., 2020) and Outer Hebrides (Orme et al., 2016) The climate parameters that storminess patterns are compared against: volcanic activity (Sigl et al., 2021)(), NH temperature evolution between latitude 30-60° (12K database, Kaufman et al., 2020), relative strength of Iceland-Scotland overflow (Thornalley et al., 2013); solar irradiance and grand solar minima periods (Steinhilber et al., 2009), July insolation at 50°N (Berger and Loutre, 1991). Climate periods discussed in the text are also indicated, warm periods in pink shading (MHT = mid-Holocene thermal maximum; RWP = roman warm period; MWP = medieval warm period) and cool periods in blue shading (BACP = bronze age cold period; DACP = dark ages cold period; LIA = little ice age), following (Goosse et al., 2006; Wanner et al., 2011, 2022; Kobashi et al., 2017; Margaritelli et al., 2020; Le Roy et al., 2024). The bar furthest right depicts the temporal division of the Holocene, following Walker et al. (2019).

Inner and Outer Hebrides). This phase of regionally enhanced storminess (~600–400 cal yr BP) coincides with one of the more pronounced cooling intervals of the Little Ice Age (LIA), attributed to combined grand solar minima and volcanic forcing (Wanner et al., 2022. Fig. 9). During this cold phase, increased storminess and aeolian activity are reported from numerous European sites (Björck and Clemmensen, 2004; Alexanderson and Fabel, 2015; Orme et al., 2015; Alexanderson and Bernhardson, 2019; Goslin et al., 2019; Sjöström et al., 2022; Kylander et al., 2023; Sjöström, 2024).

Between ~2500 and 2200 cal yr BP, the Irish sites indicate lower wind speeds, while several storm phases were inferred in the Inner Hebrides, possibly reflecting a northward displacement of the storm track. A similar pattern has been documented in other studies, suggesting that this shift affected the broader eastern North Atlantic (Bakke et al., 2008; Giraudeau et al., 2010; Orme et al., 2015).

Differences in the number of storm periods recorded at Roycarter and Glenties bogs may reflect local versus regional storm events, latitudinal shifts in storm-track position, or site-specific topographic effects. Roycarter Bog lies in an exposed coastal setting close to mineral sources (~1.5 km from beaches), whereas Glenties Bog is situated ~10 km inland within a large mire complex. Mountains rising to ~200–400 m to the southwest and southeast of Glenties Bog (Fig. 1) likely provide some shelter from winds from these directions. As Glenties Bog lies farther inland, stronger winds would be required to transport sand grains to the site. Taken together, this suggests that the storm periods identified at Glenties Bog may represent particularly intense, regionally extensive storms—mainly originating from the west or northwest.

When comparing hydrological variability between the Irish sites, two intervals of prolonged drier conditions and increased fire incidence overlapped: mid-Holocene and between 2800 and 2230 cal yr, indicating regionally drier conditions. In addition, Roycarter Bog records three further dry phases (c. 3400; 1100-800; and the last 100 cal yr BP). Previous studies show that bog size influences hydrological responsiveness, with larger bogs displaying a more subdued and delayed response to moisture changes compared with smaller systems (Sjöström et al., 2020). As Glenties Bog forms part of a large mire complex, the identified dry periods at Glenties Bog may thus represent periods of more prolonged regional drying (Fig. 8).

5.4. *Processes affecting wind- and hydroclimate in the mid- and late-Holocene*

The climate forcings that will be compared against the hydro- and wind climate in Ireland and Scotland include volcanic eruptions (Swindles et al., 2011; Sigl et al., 2021), Holocene temperature evolution (Kaufman et al., 2020), ocean circulation (Thornalley et al., 2013; Gerber et al., 2025), solar irradiance (Steinhilber et al., 2009) and orbital insolation variability (Berger and Loutre, 1991) (Fig. 9).

Holocene temperature records from Ireland and the UK are few, but those that do exist are mainly based on pollen or chironomid data and show rising temperatures in early Holocene, with peak Holocene temperatures between 8000 and 5500 cal yr BP, followed by a general decline (Blundell et al., 2008; Charman, 2010; McKeown et al., 2019; Holmes et al., 2024), in line with more recent temperature compilations (12K database, Kaufman et al., 2020, Fig. 9). The mid-Holocene warm period is mostly found in proxy records that represent summer conditions, while ice core records from Greenland (GISP2, NGRIP) and climate model projections show rapid early Holocene warming, followed by a general cooling that accelerated during the last 3000 years (Rasmussen et al., 2006; Kaufman and Broadman, 2023). When comparing events at Glenties Bog, together with the comparison sites, we find that for the early mid-Holocene generally lower wind speeds, drier conditions and peatland fires prevailed (data available from 8 ka (Co Mayo) and 7.2 ka (Co Donegal), respectively), followed by generally increasing wind speeds when temperatures start to decline (Fig. 9). A marine record, from the Norwegian sea, also inferred generally lower wind speeds and suppressed NAO index amplitude during the mid-Holocene warm period (Becker et al., 2020), supporting that reduced wind strengths prevailed during the period. Volcanic activity, as inferred from ice core reconstructions of volcanic stratospheric sulphur injections (VSSI), show elevated volcanisms occurred between c. 7600 and 5800 cal yr BP, contemporary with the mid-Holocene warm period (Fig. 9).

When turning to marine proxy reconstructions for Holocene AMOC variability, we find contrasting trends depending on location and proxy approach, indicating that there is still an incomplete understanding of past AMOC variability over millennial timescales. Nevertheless, a recent study where multiple cores where analyses for radiogenic isotopes (Pa/Th) suggest that, at least on a basin scale, AMOC strength has remained largely stable during the last 7000 years (Lippold et al., 2019; Gerber et al., 2025, Fig. 9). However, more proximal to Ireland AMOC tributaries, namely the Iceland-Scotland overflow, proxy data indicate that maximum overflow occurred around 7000 cal yr BP, followed by a decrease throughout the late Holocene. The authors associate the mid-Holocene circulation increase with an enhanced inflow of warm and saline water masses from lower latitudes, causing deeper convection (Thornalley et al., 2013). The Iceland-Scotland overflow displays an opposite trend to the Irish wind strength variability, but closely follows the NH 30-60° temperature evolution (Kaufman and et al., 2020).

In both Irish records, the mid-Holocene was characterized by relatively dry conditions, recurring fire activity, and reduced wind strength. These patterns are consistent with weakened atmospheric circulation under a warmer climate with elevated insolation (Fig. 9), when a reduced meridional temperature gradient between low and high latitudes likely limited baroclinic instability and storm-track (Wanner et al., 2008). The two mid-Holocene storm phases identified in Co. Mayo occurred during intervals when temperatures and July insolation were still elevated but had begun to decline, while solar irradiance anomalies were predominantly negative (Fig. 9). The first storm period (SP1) at Co. Mayo (SPI*:* 6150-5500 cal yr BP) was initiated directly following a period of elevated volcanism and a grand solar minima and was sustained through the mid-Holocene cool period (MHCP) (Fig. 9). The second storm period (SPII: 4970–4130 cal yr BP) also initiated following a increasedvolcanism and was sustained through the mid-Holocene warm period (MHP) and generally low volcanic activity (Fig. 9).

During the late-Holocene, when the temperature continued to decrease, the Irish records report generally wetter conditions and less fire activity compared to mid-Holocene (Fig. 9). We also note that in the late Holocene the storm periods at Glenties Bog are observed both during and in-between cold (LIA, DACP, BACP) and warm (MWP) climate phases (Fig. 9). A similar pattern was also observed in the storminess record from Roycarter Bog (Sjöström et al., 2024), suggesting that another forcing than temperature caused the increased storminess during these periods, alternatively distinct forcings affected different storm periods. When comparing the storm periods with volcanic activity, we note that during the last 1200 years, storm periods II–IV at Glenties Bog co-occurred with periods of increased Icelandic volcanic activity. Reconstruction of past Icelandic volcanic activity has shown that eruptions and ash fall over Europe have been occurring throughout the Holocene and that Icelandic volcanic activity has impacted the northern hemisphere climate throughout the Holocene (Kobashi et al., 2017). In addition, the first storm period SP1 (3415 cal yr BP) occurred directly following a peak in AAR (Fig. 9) that was dominated by tephra particles, indicating that all four storm periods identified at Glenties Bog occurred during, or just after, volcanic eruptions.

At Co Mayo (Roycarter Bog), 6 out of 9 storm periods in the late Holocene occur during phases for which volcanic activity has been reported, with no clear association between volcanisms and the two mid-Holocene storm periods were observed. Links between storminess over the British Isles and volcanisms have recently also been shown by Orme et al. (2026). The findings of this study thus further corroborate the importance of volcanisms to storminess for parts of the late-Holocene.

Explosive volcanic eruptions may effect the climate through ejecting large amounts of aerosols into the atmosphere, affecting the Earth's albedo and cooling the climate in the following years (Birkel et al., 2018). This effect might last over decades (or centuries) through sea-ice and ocean feedbacks in the northern hemisphere (Kobashi et al., 2017). In the North Atlantic region, high latitude explosive volcanic eruptions have been shown to steepen the temperature gradient, leading to increased atmospheric circulation and positive NAO patterns (Kobashi et al., 2017; Birkel et al., 2018), which could explain the elevated wind strengths and increased storminess observed over Ireland in association with volcanic eruptions. We also note that elevated volcanic activity, as recorded in ice core records (Sigl et al., 2021), does not always correspond with increased wind strengths and storminess in Ireland. This might indicate that the eruption aerosols did not reach the stratosphere and therefore had a limited cooling effect, that the storm track shifted away from our study site/s, or that the climate state at the time of the eruption governs the climatic response to the volcanic eruptions.

The results presented here suggest that distinct factors affected the wind climate during the mid-versus late-Holocene, representing distinct climate states. Variability in the temperature evolution seems to have been an important factor over centennial and millennial timescales, governing the background wind- and hydroclimate for Ireland and the UK, while volcanic activity was an important forcer during parts of the late-Holocene, operating on shorter timescales. These results shed light on climate forcings that operate on different timescales and under different climate states, which is of relevance for improving storminess predictions in a changing climate ahead.

5.5. Future studies

Future studies could couple paleostorminess reconstructions with climate modelling to further investigate the effects of volcanisms to atmospheric circulation in the eastern North Atlantic and to test how volcanic eruptions influence circulation under different climate states. To date, most paleostorminess studies have applied distinct analytical and interpretational frameworks, meaning that the definition of storm periods may be based on different criteria. Based on this, future peatland paleo-studies would benefit from applying a streamlined analytical framework. Future studies would also benefit by including pollen, particle morphology and tephra analysis. This would enable untangling the conditions under which particles where entrained and deposited, allowing identification of confounding processes. Comparing storm periods with regionally anchored temperature reconstructions would provide improved knowledge into how temperature variability influences aeolian processes.

6. Conclusions

The results from this study show that the controls on storminess and hydroclimatic variability in Ireland and western Scotland changed through the Holocene, reflecting shifts between different climate states. During the mid-Holocene warm period, low wind strengths and relatively dry conditions with recurrent fires prevailed in north-western Ireland. As temperatures began to decline, wind strengths increased, suggesting that long-term temperature evolution influenced atmospheric circulation by altering latitudinal temperature gradients and enhancing baroclinic activity.

In the late Holocene, shorter-term processes became more important. Several storm periods coincide with phases of elevated Icelandic volcanic activity, implying that explosive eruptions may have steepened meridional temperature gradients and promoted more positive NAO-like conditions across the North Atlantic. However, not all volcanic peaks align with enhanced storminess, indicating that the processes affecting storminess varied through time and climate state.

Taken together, the evidence points to temperature evolution as the key driver of long-term changes in North Atlantic storminess, with volcanic forcing acting as an intermittent amplifier, particularly during the last 1500 years. Understanding how these forcings operated under contrasting climate states provides new insight into the mechanisms controlling past atmospheric circulation and offers valuable context for interpreting how future warming may affect storm behaviour in the North Atlantic region.

Attribution for Met Éirann data use

Author contribution

Jenny Sjöström: conceptualization, lead the writing of the paper, coordination of data collection, analysis and statistical processing, interpretation and integration of results, organization of fieldwork and supervision. Antonio Martínez Cortizas: participation and supervision of FTIR analysis and statistical processing, manuscript review and editing. Andreas Nylund: participated in fieldwork, conducted sample processing, FTIR analysis and processing, result interpretations, manuscript review and editing. Frederick Schenk: result interpretation, manuscript writing, reviewing and editing. Richard Gyllencreutz: maps, result interpretation, manuscript writing, review and editing. Sanna Piilo: plant-macrofossil and charcoal analysis, manuscript reviewing and editing. Lisa Orme: result interpretation, manuscript review and editing. Michelle McKeown: manuscript reviewing and editing. Claire Ansberque: manuscript review and editing, AMOC interpretations. Malin Kylander: PI of the storminess project, acquisition of funding for analysis, staff and resources, manuscript review and editing.

Declaration of generative AI and AI-assisted technologies in the manuscript preparation process

During the preparation of this work, the author(s) used ChatGPT (OpenAI) to assist with checking sentence structure, grammar, and spelling. On occasion, ChatGPT was also used to summarise information from peer-reviewed scientific articles. The author(s) reviewed and edited all generated text as needed and take full responsibility for the content of the final manuscript.

Declaration of competing interest

The authors declare that they have no known competing financial interests or personal relationships that could have appeared to influence the work reported in this paper.

Acknowledgements

We thank Prof. S. Wastegård (Department of Physical Geography, Stockholm University) for assistance with the visual identification of tephra particles in the Glenties record. We are grateful to Meghan Windell for pre-treatment of samples and conducting the grain size analysis. We are also grateful to the Bert Bolin Centre for Climate Research for travel and analytical funding. J. Sjöström was funded by Formas (Research Council for Sustainable Development, Sweden, grant number 2020-01536), Vetenskapsrådet (the Swedish Research Council, grant number 2019-03434) and the European Union (ERC Consolidator Grant, PollutedPast, 101087832). Views and opinions expressed are however those of the author(s) only and do not necessarily reflect those of the European Union or the European Research Council. Neither the European Union nor the granting authority can be held responsible for them. M Kylander was funded by Vetenskapsrådet (grant number 2019-

03434) and FORMAS (grant number 2020-01536). A. Nylund was funded by Vetenskapsrådet (grant number 2022-04245). F. Schenk was funded by Formas (grant numbers 2020-01000 and 2023-01631). M. McKeown was funded by GSI (Geological Survey Ireland, grant number 2023-Tgc-012. C. Ansberque was funded by Formas (2022-00492).

Appendix A. Supplementary data

Supplementary data to this article can be found online at https://doi.org/10.1016/j.quascirev.2026.109901.

Data availability

Original data for this manuscript are available for download from the Bolin Centre for Climate Research repository (https://doi.org/10.17043/sjostrom-2026-ireland-1)

References

Alexanderson, H., Bernhardson, M., 2019. Late glacial and Holocene sand drift in northern götaland and Värmland, Sweden: sediments and ages. GFF 141, 84–105. https://doi.org/10.1080/11035897.2019.1582559.

Alexanderson, H., Fabel, D., 2015. Holocene chronology of the brattforsheden Delta and inland Dune field, Sw Sweden. Geochronometria 42. https://doi.org/10.1515/geochr-2015-0001.

Artz, R.R.E., Chapman, S.J., Robertson, A.H.J., Potts, J.M., Laggoun-Défarge, F., Gogo, S., Comont, L., Disnar, J.-R., Francez, A.-J., 2008. FTIR spectroscopy can predict organic matter quality in regenerating cutover peatlands. Soil Biol. Biochem. 40, 515–527.

Aubert, D., Le Roux, G., Krachler, M., Cheburkin, A., Kober, B., Shotyk, W., Stille, P., 2006. Origin and fluxes of atmospheric REE entering an ombrotrophic peat bog in Black Forest (SW Germany): evidence from snow, lichens and mosses. Geochem. Cosmochim. Acta 70, 2815–2826. https://doi.org/10.1016/j.gca.2006.02.020.

Bakke, J., Lie, Ø., Dahl, S.O., Nesje, A., Bjune, A.E., 2008. Strength and spatial patterns of the Holocene wintertime westerlies in the NE Atlantic region. Global Planet. Change 60, 28–41. https://doi.org/10.1016/j.gloplacha.2006.07.030.

Becker, L.W.M., Sejrup, H.P., Hjelstuen, B.O., Haflidason, H., Kjennbakken, H., Werner, J.P., 2020. Palaeo-productivity record from Norwegian Sea enables North Atlantic Oscillation (NAO) reconstruction for the last 8000 years. npj Clim. Atmos. Sci. 3. https://doi.org/10.1038/s41612-020-00147-6.

Berger, A., Loutre, M.F., 1991. Insolation values for the climate of the last 10 million years. Quat. Sci. Rev. 10, 297–317. https://doi.org/10.1016/0277-3791(91)90033-Q.

Biester, H., Knorr, K.-H., Schellekens, J., Basler, A., Hermanns, Y.-M., 2014. Comparison of different methods to determine the degree of peat decomposition in peat bogs. Biogeosciences 11, 2691–2707. https://doi.org/10.5194/bg-11-2691-2014.

Bindler, R., 2006. Mired in the past — looking to the future: geochemistry of peat and the analysis of past environmental changes. Global Planet. Change 53, 209–221. https://doi.org/10.1016/j.gloplacha.2006.03.004.

Birkel, S.D., Mayewski, P.A., Maasch, K.A., Kurbatov, A.V., Lyon, B., 2018. Evidence for a volcanic underpinning of the Atlantic multidecadal oscillation. npj Clim. Atmos. Sci. 1. https://doi.org/10.1038/s41612-018-0036-6.

Björck, S., Clemmensen, L.B., 2004. Aeolian sediment in raised bog deposits, Halland, SW Sweden: a new proxy record of Holocene winter storminess variation in southern Scandinavia? Holocene 14, 677–688. https://doi.org/10.1191/0959683604hl746rp.

Blaauw, M., Christen, J.A., 2011. Flexible paleoclimate age-depth models using an autoregressive gamma process. Bayesian Analysis 6, 457–474. https://doi.org/10.1214/11-BA618.

Blundell, A., Charman, D.J., Barber, K., 2008. Multiproxy late Holocene peat records from Ireland: towards a regional paleoclimate curve. J. Quat. Sci.: Published for the Quaternary Research Association 23, 59–71. https://doi.org/10.1002/jqs.1115.

Boyle, J.F., Chiverrell, R.C., Schillereff, D., 2015. Approaches to water content correction and calibration for μXRF core scanning: comparing X-ray scattering with simple regression of elemental concentrations. In: Micro-XRF Studies of Sediment Cores: Applications of a Non-destructive Tool for the Environmental Sciences. Springer, Dordrecht, pp. 373–390. https://doi.org/10.1007/978-94-017-9849-5_14.

Brayshaw, D.J., Hoskins, B., Black, E., 2010. Some physical drivers of changes in the winter storm tracks over the North Atlantic and Mediterranean during the Holocene. Philos. Trans. R. Soc. A Math. Phys. Eng. Sci. 368, 5185–5223. https://doi.org/10.1098/rsta.2010.0180.

Brayshaw, D.J., Hoskins, B., Blackburn, M., 2009. The basic ingredients of the north Atlantic storm track. Part I: Land–Sea contrast and orography. J. Atmos. Sci. 66, 2539–2558. https://doi.org/10.1175/2009JAS3078.1.

Brindley, G.W., Brown, G., 1984. Crystal structures of clay mienrals and their X-Ray identification, 5. Mineralogical Society, London, pp. 305–360, 0144-1485.

Broder, T., Blodau, C., Biester, H., Knorr, K.H., 2012. Peat decomposition records in three pristine ombrotrophic bogs in southern Patagonia. Biogeosciences 9, 1479–1491. https://doi.org/10.5194/bg-9-1479-2012.

Charman, D.J., 2010. Centennial climate variability in the British Isles during the mid-late Holocene. Quat. Sci. Rev. 29, 1539–1554.

Charman, D.J., Barber, K.E., Blaauw, M., Langdon, P.G., Mauquoy, D., Daley, T.J., Hughes, P.D.M., Karofeld, E., 2009. Climate drivers for peatland palaeoclimate records. Quat. Sci. Rev. 28, 1811–1819. https://doi.org/10.1016/j.quascirev.2009.05.013.

Constantine, M., Mooney, S., Hibbert, B., Marjo, C., Bird, M., Cohen, T., Forbes, M., McBeath, A., Rich, A., Stride, J., 2021. Using charcoal, ATR FTIR and chemometrics to model the intensity of pyrolysis: exploratory steps towards characterising fire events. Sci. Total Environ. 783, 147052. https://doi.org/10.1016/j.scitotenv.2021.147052.

Dean, W.E., 1974. Determination of Carbonate and Organic Matter in Calcareous Sediments and Sedimentary Rocks by Loss on Ignition: Comparison With Other Methods. SEPM Journal of Sedimentary Research 44, 242–248. https://doi.org/10.1306/74D729D2-2B21-11D7-8648000102C1865D.

Degen, T., Sadki, M., Bron, E., König, U., Nénert, G., 2014. The HighScore suite. Powder Diffr. 29, S13–S18. https://doi.org/10.1017/S0885715614000840.

Demsar, J., Curk, T., Curk, T., Erjavec, A., Erjave, A., 2013. Orange: data mining toolbox in python. J. Mach. Learn. Res. 14, 2349–2353. https://doi.org/10.5555/2567709.2567736.

Doskočil, L., Enev, V., Pekař, M., Wasserbauer, J., 2016. The spectrometric characterization of lipids extracted from lignite samples from various coal basins. Organic Geochemistry 95, 34–40. https://doi.org/10.1016/j.orggeochem.2016.02.008.

EMODnet, 2024. EMODnet Digital bathymetry. https://doi.org/10.12770/cf51df64-56f9-4a99-b1aa-36b8d7b743a1.

Environmental Protection Agency, 2024. Updated High-Resolution Climate Projections for Ireland. Research Report: Environmental Protection Agency EPA Research Programme, p. 133, 2021-2030. https://www.epa.ie/publications/research/epa-research-2030-reports/Research_Report-471-1.pdf.

Eriksson, L., Johansson, E., Katteneh-Wodl, N., Wold, S., 1999. Introduction to Multi- and Megavariate Data Analysis Using Projection Methods (PCA & PLS): Umeå, Umetrics AB.

Essell, H., Plunkett, G., Blaauw, M., 2025. Challenges in dating blanket peat and implications for understanding its initiation in Ireland. J. Quat. Sci. https://doi.org/10.1002/jqs.3723 jqs.3723.

EU-DEM, 2025. Copernicus DEM - global and European digital elevation model GLO-30. https://doi.org/10.5270/ESA-c5d3d65.

Feser, F., Barcikowska, M., Krueger, O., Schenk, F., Weisse, R., Xia, L., 2015. Review Article Storminess over the North Atlantic and northwestern Europe – a review. Q. J. R. Meteorol. Soc. 141, 350–382. https://doi.org/10.1002/qj.2364.

Feser, F., Krueger, O., Woth, K., Van Garderen, L., 2021. North Atlantic Winter storm activity in modern reanalyses and pressure-based observations. J. Clim. 34, 2411–2428. https://doi.org/10.1175/JCLI-D-20-0529.1.

Fossit, J.A., 1994. Late-Glacial and Holocene Vegetation History of Western Donegal, Ireland: Biology and Environmental, 94B. Proceedings of the Royal Irish Academy, pp. 1–31.

Friedman, G.M., Sanders, J.E., 1978. Principles of Sedimentology, 4. Wiley, New York, pp. 792–p.. https://doi.org/10.1002/esp.3290040317.

Gallego-Sala, A.V., Colin Prentice, I., 2013. Blanket peat biome endangered by climate change. Nat. Clim. Change 3, 152–155. https://doi.org/10.1038/nclimate1672.

Gao, C., Cong, J., Sun, Y., Han, D., Wang, G., 2022. Variability in pyrogenic carbon properties generated by different burning temperatures and peatland plant litters: implication for identifying fire intensity and fuel types. Int. J. Wildland Fire 31, 395–408. https://doi.org/10.1071/WF21053.

Gerber, L., et al., 2025. Low variability of the Atlantic Meridional Overturning Circulation throughout the Holocene. Nat. Commun. 16, 6748. https://doi.org/10.1038/s41467-025-61793-z.

Giraudeau, J., Grelaud, M., Solignac, S., Andrews, J.T., Moros, M., Jansen, E., 2010. Millennial-scale variability in Atlantic water advection to the Nordic Seas derived from Holocene coccolith concentration records. Quat. Sci. Rev. 29, 1276–1287. https://doi.org/10.1016/j.quascirev.2010.02.014.

Givelet, N., et al., 2004. Suggested protocol for collecting, handling and preparing peat cores and peat samples for physical, chemical, mineralogical and isotopic analyses. Journal of Environmental Monitoring 6, 481–492. https://doi.org/10.1039/B401601G.

Goslin, J., Gałka, M., Sander, L., Fruergaard, M., Mokenbusch, J., Thibault, N., Clemmensen, L.B., 2019. Decadal variability of north-eastern Atlantic storminess at the mid-Holocene: new inferences from a record of wind-blown sand, western Denmark. Global Planet. Change 180, 16–32. https://doi.org/10.1016/j.gloplacha.2019.05.010.

Hodgkins, S.B., Tfaily, M.M., McCalley, C.K., Logan, T.A., Crill, P.M., Saleska, S.R., Rich, V.I., Chanton, J.P., 2014. Changes in peat chemistry associated with permafrost thaw increase greenhouse gas production. Proceedings of the National Academy of Sciences 111, 5819–5824. https://doi.org/10.1073/pnas.1314641111.

Holmes, J.A., Tindall, J., Jones, M., Holloway, M., Roberts, N., Feeser, I., 2024. Climate and atmospheric circulation during the early and Mid-Holocene inferred from lake-carbonate oxygen-isotope records from western Ireland. J. Quat. Sci. 39, 24–36. https://doi.org/10.1002/jqs.3571.

Hooper, J., 2018. A global doubling of dust emissions during the Anthropocene? Global Planet. Change 22.

Hurrell, J.W., Van Loon, H., 1997. Decadal variations in climate assoicated with the north Atlantic oscillation. Clim. Change 36, 26.

IPCC, 2021. Climate Change 2021 – the Physical Science Basis: Working Group I Contribution to the Sixth Assessment Report of the Intergovernmental Panel on Climate Change. Cambridge University Press. https://doi.org/10.1017/9781009157896.

Kaufman, D.S., Broadman, E., 2023. Revisiting the Holocene global temperature conundrum. Nature 614, 425–435. https://doi.org/10.1038/s41586-022-05536-w.

Kaufman, D., et al., 2020. A global database of Holocene paleotemperature records. Sci. Data 7, 34. https://doi.org/10.1038/s41597-020-0445-3.

Kidston, J., Scaife, A.A., Hardiman, S.C., Mitchell, D.M., Butchart, N., Baldwin, M.P., Gray, L.J., 2015. Stratospheric influence on tropospheric jet streams, storm tracks and surface weather. Nature Geoscience 8, 433–440. https://doi.org/10.1038/ngeo2424.

Kirby, J.R., Garrett, E., Gehrels, W.R., 2023. Holocene relative sea-level changes in northwest Ireland: an empirical test for glacial isostatic adjustment models. Holocene 33, 926–938. https://doi.org/10.1177/09596836231169992.

Klavans, J.M., Cane, M.A., Clement, A.C., Murphy, L.N., 2021. NAO predictability from external forcing in the late 20th century. npj Clim. Atmos. Sci. 4, 22. https://doi.org/10.1038/s41612-021-00177-8.

Kobashi, T., et al., 2017. Volcanic influence on centennial to millennial Holocene Greenland temperature change. Sci. Rep. 7, 1441. https://doi.org/10.1038/s41598-017-01451-7.

Kuchar, J., Milne, G., Hubbard, A., Patton, H., Bradley, S., Shennan, I., Edwards, R., 2012. Evaluation of a numerical model of the British–Irish ice sheet using relative sea-level data: implications for the interpretation of trimline observations. J. Quat. Sci. 27, 597–605. https://doi.org/10.1002/jqs.2552.

Kylander, M.E., et al., 2023. Storm chasing: tracking Holocene storminess in southern Sweden using mineral proxies from inland and coastal peat bogs. Quat. Sci. Rev. 299, 107854. https://doi.org/10.1016/j.quascirev.2022.107854.

Kylander, M.E., Klaminder, J., Wohlfarth, B., Löwemark, L., 2013. Geochemical responses to paleoclimatic changes in southern Sweden since the late glacial: the Hässeldala Port lake sediment record. J. Paleolimnol. 50, 57–70. https://doi.org/10.1007/s10933-013-9704-z.

Kylander, M.E., Martínez-Cortizas, A., Bindler, R., Greenwood, S.L., Mörth, C.-M., Rauch, S., 2016. Potentials and problems of building detailed dust records using peat archives: an example from Store Mosse (the "Great Bog"), Sweden. Geochem. Cosmochim. Acta 190, 156–174. https://doi.org/10.1016/j.gca.2016.06.028.

Kylander, M.E., Söderlindh, J., Schenk, F., Gyllencreutz, R., Rydberg, J., Bindler, R., Martínez Cortizas, A., Skelton, A., 2020. It's in your glass: a history of sea level and storminess from the Laphroaig bog, Islay (southwestern Scotland). Boreas 49, 152–167. https://doi.org/10.1111/bor.12409.

Larsen, G., Dugmore, A.J., Newton, A.J., 1999. Geochemistry of historic silicic tephras in Iceland. Holocene 9, 463–471.

Larsen, G., þórarinsson, S., 1977. H4 and Other Acid Hekla Tephra Layers: Jökull, vol. 27, pp. 28–46.

Le Roux, G., Laverret, E., Shotyk, W., 2006. Fate of calcite, apatite and feldspars in an ombrotrophic peat bog, Black Forest, Germany. J. Geol. Soc. 163, 641–646. https://doi.org/10.1144/0016-764920-035.

Le Roy, M., Ivy-Ochs, S., Nicolussi, K., Monegato, G., Reitner, J.M., Colucci, R.R., Ribolini, A., Spagnolo, M., Stoffel, M., 2024. Holocene glacier variations in the Alps. In: European Glacial Landscapes. Elsevier, The European glacial landforms during the Holocene, pp. 367–418. https://doi.org/10.1016/B978-0-323-99712-6.00018-0.

Lieffers, V., MacDonald, E., 1989. Growth and foliar nutrient status of black spruce and tamarack in relation to depth of water table in some Alberta peatlands. Can. J. For. Res. 20, 805–809. https://doi.org/10.1139/x90-106.

Lippold, J., et al., 2019. Constraining the variability of the Atlantic meridional overturning circulation during the Holocene. Geophys. Res. Lett. 46, 11338–11346. https://doi.org/10.1029/2019GL084988.

Malmer, N., 1988. Patterns in the growth and the accumulation of inorganic constituents in the sphagnum cover on ombrotrophic bogs in Scandinavia. Oikos 53, 105. https://doi.org/10.2307/3565670.

Manning, C., Kendon, E.J., Fowler, H.J., Roberts, N.M., 2023. Projected increase in windstorm severity and contribution from sting jets over the UK and Ireland. Weather Clim. Extrem., 100562 https://doi.org/10.1016/j.wace.2023.100562.

Margaritelli, G., Cacho, I., Català, A., Barra, M., Bellucci, L.G., Lubritto, C., Rettori, R., Lirer, F., 2020. Persistent warm Mediterranean surface waters during the Roman period. Sci. Rep. 10, 10431. https://doi.org/10.1038/s41598-020-67281-2.

Martínez Cortizas, A., Mighall, T., Pontevedra Pombal, X., Nóva Muñfoz, J.C., Peiteado Varelal, E., Piñero Rebolol, R., 2005. Linking changes in atmospheric dust deposition, vegetation change and human activities in northwest Spain during the last 5300 years. Holocene 15, 698–706. https://doi.org/10.1191/0959683605hl834rp.

Martínez Cortizas, A., Sjöström, J.K., Ryberg, E.E.S., Kylander, M.E., Kaal, J., López-Costas, O., Bindler, R., 2021. 9000 years of change in peat organic matter composition in Store Mosse (Sweden) traced using FTIR-ATR. Boreas 50, 1161–1178. https://doi.org/10.1111/bor.12527.

Martínez Cortizas, A., Traoré, M., López-Costas, O., Sarret, G., Guédron, S., 2025. Early peat diagenesis controls on bromine accumulation. Soil Syst. 9, 120. https://doi.org/10.3390/soilsystems9040120.

Martínez Cortizas, A., Vázquez, C.F., Kaal, J., Biester, H., Casais, M.C., Rodríguez, T.T., Lado, L.R., 2016. Bromine accumulation in acidic black colluvial soils. Geochem. Cosmochim. Acta 174, 143–155. https://doi.org/10.1016/j.gca.2015.11.013.

Mauquoy, D., Hughes, P.D.M., van Geel, B., 2010. A protocol for plant macrofossil analysis of peat deposits: Mires and Peat, pp. 1–5.

Mauquoy, D., van Geel, B., 2007. Plant macrofossil method and studies: Mire and Peat Macros (Scott Elias. In: Encyclopedia of Quaternary Science, 3. Elsevier, pp. 2315–2336. https://doi.org/10.1016/B0-44-452747-8/00229-5.

McKeown, M.M., Caseldine, C.J., Thompson, G., Swindles, G.T., Ivanovic, R.F., Roland, T.P., Valdes, P.J., Potito, A.P., 2019. Complexities in interpreting chironomid-based temperature reconstructions over the Holocene from a lake in Western Ireland. Quat. Sci. Rev. 222, 105908. https://doi.org/10.1016/j.quascirev.2019.105908.

Met Éirann, 2024. Annual averages 2011-2023 CE. Finner weather station: https://www.met.ie/climate/available-data/historical-data.

Moore, M.D., Reynolds, C.R., 1997. X-ray Diffraction and the Identification and Analysis of Clay Minerals. Oxford University Press, Oxford, UK, p. 332.

Moreno, F., Moreno, J., Fatela, F., Guise, L., Vieira, C., Leira, M., 2020. Bromine biogeodynamics in the NE Atlantic: a perspective from natural wetlands of western Portugal. Sci. Total Environ. 722, 137649. https://doi.org/10.1016/j.scitotenv.2020.137649.

Nesse, W.D., 2017. Introduction to Mineralogy. Oxford University Press, New York.

Orme, L.C., et al., 2026. Storminess in north west Europe and volcanic activity during the Holocene. Clim. Past 22, 287–313. https://doi.org/10.5194/cp-22-287-2026.

Orme, L.C., Davies, S.J., Duller, G.A.T., 2015. Reconstructed centennial variability of late Holocene storminess from Cors Fochno, Wales, UK. J. Quat. Sci. 30, 478–488. https://doi.org/10.1002/jqs.2792.

Orme, L.C., Reinhardt, L., Jones, R.T., Charman, D.J., Barkwith, A., Ellis, M.A., 2016. Aeolian sediment reconstructions from the Scottish Outer Hebrides: late Holocene storminess and the role of the North Atlantic Oscillation. Quat. Sci. Rev. 132, 15–25. https://doi.org/10.1016/j.quascirev.2015.10.045.

Pilcher, J.R., Hall, V.A., McCORMAC, F.G., 1996. An outline tephrochronology for the Holocene of the north of Ireland. J. Quat. Sci. 11, 485–494. https://doi.org/10.1002/(SICI)1099-1417(199611/12)11:6%3C485::AID-JQS266%3E3.0.CO;2-T.

Pinto, J.G., Zacharias, S., Fink, A.H., Leckebusch, G.C., Ulbrich, U., 2009. Factors contributing to the development of extreme North Atlantic cyclones and their relationship with the NAO. Climate Dynamics 32, 711–737. https://doi.org/10.1007/s00382-008-0396-4.

Pye, K., 1987. Aeolian Dust and Dust Deposits. Academic Press, London, p. 334. https://doi.org/10.1016/B978-0-12-568690-7.50001-6.

Rasmussen, S.O., et al., 2006. A new Greenland ice core chronology for the last glacial termination. J. Geophys. Res. Atmos. 111, e006079. https://doi.org/10.1029/2005JD006079.

Reimer, P.J., et al., 2020. The IntCal20 Northern hemisphere radiocarbon Age calibration curve (0–55 cal kBP). Radiocarbon 62, 725–757. https://doi.org/10.1017/RDC.2020.41.

Rietveld, 1969. A profile refinement method for nuclear and magnetic structures. J. Appl. Crystallogr. 2. https://doi.org/10.1107/S0021889869006558.

Shennan, I., 2018. Relative sea-level changes and crustal movements in Britain and Ireland since the last Glacial Maximum. Quat. Sci. Rev. 188, 143–159. https://doi.org/10.1016/j.quascirev.2018.03.031.

Shotyk, W., Krachler, M., Martinez-Cortizas, A., Cheburkin, A.K., Emons, H., 2002. A peat bog record of natural, pre-anthropogenic enrichments of trace elements in atmospheric aerosols since 12 370 14 C yr BP, and their variation with Holocene climate change. Earth Planet Sci. Lett. 199, 21–37. https://doi.org/10.1016/S0012-821X(02)00553-8.

Sigl, M., Toohey, M., McConnell, J.R., Cole-Dai, J., Severi, M., 2021. HolVol: Reconstructed Volcanic Stratospheric Sulfur Injections and Aerosol Optical Depth for the Holocene (9500 BCE to 1900 CE), p. 2. https://doi.org/10.1594/PANGAEA.928646 data points.

Silva-Sánchez, N., Martínez Cortizas, A., López-Merino, L., 2014. Linking forest cover, soil erosion and mire hydrology to late-holocene human activity and climate in NW Spain. Holocene 24, 714–725. https://doi.org/10.1177/0959683614526934.

Sjöström, J.K., 2024. Mid-Holocene paleostorminess in north-western Ireland inferred from grain size, mineral and molecular content. Gothenburg, Geologiska Föreningen Specialpublikation 5, 558.

Sjöström, J.K., Bindler, R., Cortizas, A.M., Björck, S., Karlsson, A., Ellerton, D.T., Kylander, M.E., 2022. Late Holocene peat paleodust deposition in south-western Sweden - exploring geochemical properties, local mineral sources and regional aeolian activity. Chem. Geol. 602, 37. https://doi.org/10.1016/j.chemgeo.2022.120881.

Sjöström, J.K., Bindler, R., Granberg, T., Kylander, M.E., 2019. Procedure for Organic Matter Removal from Peat Samples for XRD Mineral Analysis: Wetlands, vol. 39, pp. 473–481. https://doi.org/10.1007/s13157-018-1093-7.

Sjöström, J.K., Gyllencreutz, R., Martínez Cortizas, A., Nylund, A., Piilo, S.R., Schenk, F., McKeown, M., Ryberg, E.E., Kylander, M.E., 2024. Holocene storminess dynamics in northwestern Ireland: shifts in storm duration and frequency between the mid- and late Holocene. Quat. Sci. Rev. 337, 108803. https://doi.org/10.1016/j.quascirev.2024.108803.

Sjöström, J.K., Martínez Cortizas, A., Hansson, S.V., Silva Sánchez, N., Bindler, R., Rydberg, J., Mörth, C.-M., Ryberg, E.E.S., Kylander, M.E., 2020. Paleodust deposition and peat accumulation rates – bog size matters. Chem. Geol. 504, 119795. https://doi.org/10.1016/j.chemgeo.2020.119795.

Steinhilber, F., Beer, J., Frölich, C., 2009. Total solar irradiance during the Holocene. Geophys. Res. Lett. 36. https://doi.org/10.1029/2009GL040142,%202009.

Steinmann, P., Shotyk, W., 1997. Geochemistry, mineralogy, and geochemical mass balance on major elements in two peat bog profiles (Jura Mountains, Switzerland). Chem. Geol. 138, 25–53. https://doi.org/10.1016/S0009-2541(96)00171-4.

Swindles, G.T., Lawson, I.T., Savov, I.P., Connor, C.B., Plunkett, G., 2011. A 7000 Yr Perspective on Volcanic Ash Clouds Affecting Northern Europe: Geology, vol. 39, pp. 887–890. https://doi.org/10.1130/G32146.1.

Thornalley, D.J.R., Blaschek, M., Davies, F.J., Praetorius, S., Oppo, D.W., McManus, J.F., Hall, I.R., Kleiven, H., Renssen, H., McCave, I.N., 2013. Long-term variations in Iceland–Scotland overflow strength during the Holocene. Clim. Past 9, 2073–2084. https://doi.org/10.5194/cp-9-2073-2013.

Torbenson, M.C.A., Plunkett, G., Brown, D.M., Pilcher, J.R., Leuschner, H.H., 2015. Asynchrony in key Holocene chronologies: evidence from Irish bog pines. Geology 43, 799–802. https://doi.org/10.1130/G36914.1.

Trigo, R.M., Osborn, T.J., Corte-Real, J.M., 2002. The North Atlantic Oscillation influence on Europe: climate impacts and assoicated physical mechanisms. Climate Research 20, 9–17. https://doi.org/10.3354/cr020009.

Uhelski, D.M., Kane, E.S., Chimner, R.A., Heckman, K.A., Miesel, J., Xie, L., 2022. Pyrogenic carbon content of Sphagnum peat soils estimated using diffuse reflectance FTIR spectrometry. Mires Peat 28, 1–22. https://doi.org/10.19189/MaP.2022.OMB.StA.2420.

Väliranta, M., Korhola, A., Seppä, H., Tuittila, E.-S., Sarmaja-Korjonen, K., Laine, J., Alm, J., 2007. High-resolution reconstruction of wetness dynamics in a southern boreal raised bog, Finland, during the late Holocene: a quantitative approach. The Holocene 17, 1093–1107. https://doi.org/10.1177/0959683607082550.

Vandenberghe, J., 2013. Grain size of fine-grained windblown sediment: a powerful proxy for process identification. Earth Sci. Rev. 121, 18–30. https://doi.org/10.1016/j.earscirev.2013.03.001.

Walker, M., et al., 2019. Formal subdivision of the Holocene Series/Epoch: a Summary. J. Geol. Soc. India 93, 135–141. https://doi.org/10.1007/s12594-019-1141-9.

Walter, K., Graf, 2005. The North Atlantic variability structure, storm tracks, and precipitation depending on the polar vortex strength. Atmospheric Chemistry and Physics 239–248.

Wanner, H., et al., 2008. Mid- to late Holocene climate change: an overview. Quat. Sci. Rev. 27, 1791–1828. https://doi.org/10.1016/j.quascirev.2008.06.013.

Wanner, H., Pfister, C., Neukom, R., 2022. The variable European Little Ice Age. Quat. Sci. Rev. 287, 107531. https://doi.org/10.1016/j.quascirev.2022.107531.

Wanner, H., Solomina, O., Grosjean, M., Ritz, S.P., Jetel, M., 2011. Structure and origin of Holocene cold events. Quat. Sci. Rev. 30, 3109–3123. https://doi.org/10.1016/j.quascirev.2011.07.010.

Wastegård, S., 2005. Late Quaternary tephrochronology of Sweden: a review. Quat. Int. 130, 49–62. https://doi.org/10.1016/j.quaint.2004.04.030.

Wohlfarth, B., Skog, G., Possnert, G., Holmquist, B., 1998. Pitfalls in the AMS radiocarbon-dating of terrestrial macrofossils. JOURNAL OF QUATERNARY SCIENCE 13, 9.

Zaccone, C., Rein, G., D'Orazio, V., Hadden, R.M., Belcher, C.M., Miano, T.M., 2014. Smouldering fire signatures in peat and their implications for palaeoenvironmental reconstructions. Geochem. Cosmochim. Acta 137, 134–146. https://doi.org/10.1016/j.gca.2014.04.018.

Geological Survey of Ireland, 2024, Geological Survey of Ireland Spatial Resources:, https://www.gsi.ie/en-ie/data-and-maps/Pages/default.aspx. Accessed: 2025-02-02.

Hurrell, J.W., Philips, A., and National Center for Atmospheric Research Staff, 2024, The Climate Data Guide: Hurrell North Atlantic Oscillation (NAO) Index (PC-based):, https://climatedataguide.ucar.edu/climate-data/hurrell-north-atlantic-oscillation-nao-index-pc-based (accessed February 2024).

Goosse, H., Arzel, O., Luterbacher, J., Mann, M.E., Renssen, H., Riedwyl, N., Timmermann, A., Xoplaki, E., and Wanner, H., 2006, The origin of the European "Medieval Warm Period": Climate of the Past, v. 2, p. 99–113, doi:https://doi.org/10.5194/cp-2-99-2006, 2006.